Computational Role of Tunneling in a Programmable Quantum Annealer

Sergio Boixo[1], Vadim N. Smelyanskiy[2], Alireza Shabani[1], Sergei V. Isakov[1], Mark Dykman[3], Mohammad Amin[4], Masoud Mohseni[1], Vasil S. Denchev[1], Hartmut Neven[1]

[1] *Google*

[2] *NASA Ames*

[3] *Physics and Astronomy Department, Michigan State University*

[4] *D-Wave Systems*

Quantum tunneling is a phenomenon in which a quantum state tunnels through energy barriers above the energy of the state itself [1]. Tunneling has been hypothesized as an advantageous physical resource for optimization [2–6]. Here we present the first experimental evidence of a computational role of multiqubit quantum tunneling in the evolution of a programmable quantum annealer. We developed a theoretical model based on a NIBA Quantum Master Equation to describe the multiqubit dissipative cotunneling effects under the complex noise characteristics of such quantum devices. We start by considering a computational primitive, the simplest non-convex optimization problem consisting of just one global and one local minimum. The quantum evolutions enable tunneling to the global minimum while the corresponding classical paths are trapped in a false minimum. In our study the non-convex potentials are realized by frustrated networks of qubit clusters with strong intra-cluster coupling. We show that the collective effect of the quantum environment is suppressed in the "critical" phase during the evolution where quantum tunneling "decides" the right path to solution. In a later stage dissipation facilitates the multiqubit cotunneling leading to the solution state. The predictions of the model accurately describe the experimental data from the D-Wave II quantum annealer at NASA Ames. In our computational primitive the temperature dependence of the probability of success in the quantum model is opposite to that of the classical paths with thermal hopping. Specifically, we provide an analysis of an optimization problem with sixteen qubits, demonstrating eight qubit cotunneling that increases success probabilities. Furthermore, we report results for larger problems with up to 200 qubits that contain the primitive as subproblems.

I. INTRODUCTION

Quantum tunneling was discovered in the late 1920s to explain field electron emission in vacuum tubes. Today this phenomenon is at the core of many essential technological innovations such as the tunnel field-effect transistor, field emission displays and the scanning tunneling microscope. Tunneling is also at the heart of energy and charge transport in biological and chemical processes. Recently cotunneling effects involving multiple quantum mechanical particles have been used to develop single electron transistors and hypersensitive measurement instruments.

Quantum tunneling, in particular for thin but high energy barriers, has been hypothesized as an advantageous mechanism for quantum optimization [2–6]. In classical simulated annealing or cooling optimization algorithms, the corresponding temperature parameter must be raised to overcome energy barriers. But if there are many potential local minima with smaller energy differences than the height of the barrier, the temperature must also be lowered to distinguish between them so the algorithm can converge to the global minimum. Quantum tunneling is present even at zero-temperature. Therefore, for some energy landscapes, one might expect that quantum dynamical evolutions can converge to the global minimum faster than classical optimization algorithms. Quantum annealing [2, 3] is a technique inspired by classical annealing but designed to take advantage of quantum tunneling. Single qubit quantum tunneling for a programmable annealer has been demonstrated experimentally in Ref. [7], and two qubit cotunneling has been detected indirectly using microscopic resonant tunneling in Ref. [8] (see below).

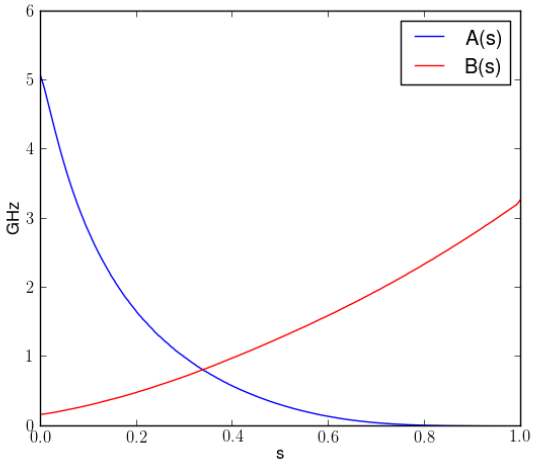

FIG. 1. Quantum annealing functions $A(s)$ and $B(s)$. The function $A(t)$ is defined as twice the median energy difference between the two lowest eigenstates of the experimentally superconducting flux qubit. The function $B(s)$ is defined as 1.41 pico henries times the square of the persistent current $I_p^2(s)$, as explained in App. II B.

The state evolution in transverse field quantum annealing is governed by a time dependent Hamiltonian

of the form [9]

$$H_0(s) = A(s)H^{\rm D} + B(s)H^{\rm P} \quad (1)$$

$$H^{\rm D} = -\sum_{\mu} \sigma_{\mu}^{x} \quad (2)$$

$$H^{\rm P} = -\sum_{\mu} h_{\mu}\sigma_{\mu}^{z} - \sum_{\mu\nu} J_{\mu\nu}\sigma_{\mu}^{z}\sigma_{\nu}^{z} \, . \quad (3)$$

Here $H^{\rm D}$ is the driver Hamiltonian, $H^{\rm P}$ is the problem Hamiltonian whose ground state is the solution of an optimization problem of interest, $\{\sigma_{\mu}^{x}, \sigma_{\mu}^{z}\}$ are Pauli matrices acting on spin μ, $s = t/t_{qa}$ is the annealing parameter, and t_{qa} is the duration of the quantum annealing process. The functions $A(s)$ and $B(s)$ used in the rest of the paper are shown in Fig. 1. The Hamiltonian path $H_0(s)$ describes an evolution of effective 2-level spin systems (qubits) from an initial phase with a unique ground state to a final Hamiltonian with eigenstates aligned with the z quantization axis. In the initial unique ground state all the qubits are aligned with the effective transverse magnetic field in the x direction. See Appendix A for a more complete derivation of the single qubit Hamiltonian and the parameteres the experimental system considered in this paper.

Closed system quantum adiabatic evolutions governed by the time-dependent Hamiltonian given in Eq. (1) will arrive at the final ground state of the problem Hamiltonian if the total evolution time is large compared to the inverse minimum energy gap along the Hamiltonian path [9]. In this paper we shall analyze the performance of a quantum annealing device with superconducting flux qubits [7, 10, 11]. The qubits are coupled inductively in a connectivity graph that is formed by a grid of cells with high internal connectivity. The qubits are subject to interaction with the environment with the dominant noise source being spin diffusion at the superconductor insulator interface [12–14]. This is known to produce control errors, energy level broadening as well as thermal excitation and relaxation [15, 16]. The noise characteristics of individual qubits have been studied in macroscopic resonant tunneling experiments [17]. We show nevertheless that even under such conditions the device performance can benefit from multiqubit cotunneling of strongly interacting qubit clusters. This is of relevance for current programmable quantum annealers, such as the D-Wave II chip at NASA Ames.

In this work we design an Ising model implementation with 16 qubits of a computational primitive, the simplest non-convex optimization problem consisting of just one global and one local minimum. The final global minimum can only be reached by traversing an energy barrier. We develop a NIBA Quantum Master Equation which takes high and low frequency noise into account. Our comprehensive open quantum system modeling, with close agreement with D-Wave machine output, demonstrates how cotunneling can exist and play a functional role in presence of both Ohmic and strong $1/f$ noise components affecting coherence of the flux qubits. Independent of specific choices in the quantum models or the classical models, the prediction is that the probabilities to find the system in the lowest energy state should decrease with increasing temperature for a quantum system but should increase for a classical system. This is indeed observed, demonstrating eight qubit cotunneling that increases success probabilities. We compare with physically plausible models of the hardware that only employ product states which do not allow for multiqubit tunneling transitions. Experimentally we find that for this situation the D-Wave II processor returns the solution that minimizes the energy with higher probability than these models. Beyond the original 16 qubit probe problem we also explore larger problems that contain multiple weak-strong cluster pairs.

II. A PRIMITIVE "PROBE" PROBLEM CHARACTERIZED BY A DOUBLE WELL POTENTIAL

A. The quantum Hamiltonian

The archetypal primitive to study quantum tunneling is a double-well potential: two local minima separated by an energy barrier. Our aim is to distinguish quantum tunneling from thermal activation in a model using classical paths. Classical paths are limited to local spin vector dynamics over product states to get over the energy barrier. In contrast, the signature of a quantum system is that entangled states are available as well. We utilize qubit networks of the D-Wave 2 quantum annealer chip at NASA Ames to design time dependent asymmetric double well potentials where a classical path continuously connects the initial global minimum to the final false minimum. In this way one can study how the system escapes the local minimum and traverses the energy barrier to reach the global optimum. We will see that quantum tunneling results in a different final probability of success than the corresponding classical dynamics over classical paths. We compare the experimental data from the device with numerical simulations of classical paths and with the predictions of a comprehensive analytical model for dissipative multiqubit cotunneling. Based on the results of this comparison, we establish the functional role of tunneling in the evolution on a programmable quantum annealer.

We now detail how the double well potential and time evolution can be constructed in the case of network graphs with finite connectivity. We will focus on the particular case of the so-called Chimera graph that connects the qubits in the current D-Wave II architecture, although similar constructions can be applied to more general network architectures. We choose our double well primitive probe problem to be the one depicted in Fig. 2. We use two Chimera cells, each with $n = 8$ qubits. We find it useful during our analysis to keep n explicit. We will choose equal local fields for the spins within each cell. We also choose all the couplings to be equal and ferromagnetic. There are $n^2/4$ *intra*-cell couplings and $n/2$ *inter*-cell couplings. The spins within each cell tend to move together as an homogenous cluster because flipping only one spin rises the energy by an amount $\propto nJ$ which is much

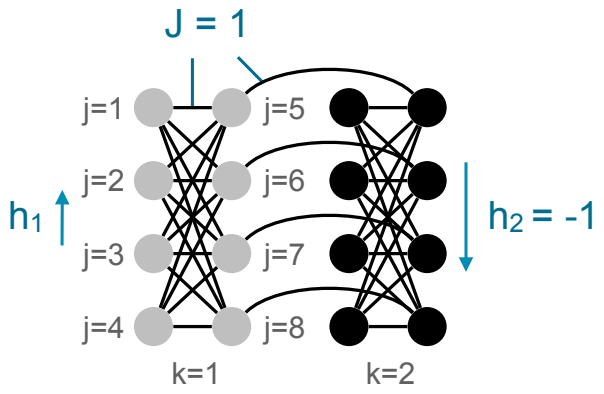

FIG. 2. The probe problem under study, consisting of 16 qubits in two unit cells of the so-called Chimera graph. All qubits are ferromagnetically coupled and evolve as two distinct qubit clusters. At the end of the annealing evolution the right cluster is strongly pinned downward due to strong local fields acting on all qubits in that cell. The local magnetic field h_1 in the left cluster is weaker however, and serves as a bifurcation parameter. For $h_1 < J/2$ the left cluster will reverse its orientation during the annealing sweep and eventually align itself with the right cluster. Note the permutation symmetry in each column which allows us to adopt the large spin description.

greater than the energy of the inter-cell bond $\propto 2J$. The problem Hamiltonian is of Ising form

$$H^{\rm P} = H_1^{\rm P} + H_2^{\rm P} + H_{1,2}^{\rm P} \tag{4}$$

$$H_k^{\rm P} = -J \sum_{\langle j,j'\rangle \in {\rm intra}} \sigma_{j,k}^z \sigma_{j',k}^z - \sum_{j=1}^{n} h_k\, \sigma_{j,k}^z \tag{5}$$

$$H_{1,2}^{\rm P} = -J \sum_{j\in {\rm inter}} \sigma_{j,1}^z \sigma_{j,2}^z \,. \tag{6}$$

The index $k \in \{1,2\}$ denotes the Chimera cell, the first sum in (5) goes over the *intra*-cell couplings depicted in Fig. 2, and the second sum goes over the *inter*-cell couplings corresponding to $j \in (n/2+1, n)$ in Fig. 2; h_k denotes the local fields within each cell.

Toward the end of quantum annealing the problem Hamiltonian $H^{\rm P}$ is dominating the evolution and $\langle \sigma_{j,k}^z \rangle \simeq \pm 1$ where $\langle \ldots \rangle$ denotes a quantum mechanical average. We choose the local fields to point in opposite directions. For simplicity we set the largest magnitude field $h_2 = -J$ (the largest magnitude field). We further choose $J > h_1 > 0$. If $h_1 < J/2$ then the global minimum corresponds to the qubits in both clusters polarized in the same direction as the largest field, h_2. There also exists a "false" minimum corresponding to the clusters oriented in the opposite directions (each along its own local field).

We now explain the onset of the frustration in this system. We observe that at the beginning of quantum annealing

$$\langle \sigma_{j,k}^z \rangle \simeq h_k\, B(s)/A(s), \qquad B(s)/A(s) \ll 1 \,. \tag{7}$$

The Ising coupling terms in the problem Hamiltonian (5) are quadratic while the local field terms are linear in z-polarizations. Therefore at the beginning of quantum annealing the effect of the local z-fields dominates that of the *inter*-cell Ising couplings. According to (7), because h_1 and h_2 have the opposite signs so will the z-projections of the spins $\langle \sigma_{j,k}^z \rangle$ in the two clusters early in the evolution.

A key observation is that in the absence of quantum tunneling and thermal hoping the spin projection of the two clusters stay opposite during the evolution arriving to the false minimum with residual energy relative to the global minimum equal to $n(J - 2h_1)$. The system will get trapped into the false minimum. To escape it all spins in the left cluster must flip the sign which requires going over the barrier top. At the tipping point of the barrier the left cluster has zero total z-polarization and therefore the barrier grows with the ferromagnetic energy of the cluster $(n/2)^2 J$. For sufficiently large n the barrier height $\mathcal{O}(n^2)$ is much greater than the residual energy $\mathcal{O}(n)$. It will be shown below that in certain region of the annealing parameter s all qubits in the left cluster will tunnel in a concerted motion under the energy barrier separating the two potential wells that correspond to the opposite z-polarizations of the cluster.

Next, we discuss an approximation which reduces the size of the Hamiltonian matrix for the 2 unit cell problem from 2^{2n} to $(n/4+1)^4$. We introduce total spin operators for each column of a unit cell (cf. Fig. 2)

$$S_{k,1}^\alpha = \frac{1}{2}\sum_{j=1}^{n/2} \sigma_{j,k}^\alpha \,, \quad S_{k,2}^\alpha = \frac{1}{2}\sum_{j=n/2+1}^{n} \sigma_{j,k}^\alpha \,, \tag{8}$$

where $\alpha \in x, y, z$, and $k \in \{1,2\}$ denotes the left and right Chimera cells. Because the intra-cell Hamiltonians (5) and the driver Hamiltonian are symmetric with respect to qubit permutations they can be written in terms of the total spin operators

$$H_k^{\rm P} = -4J S_{k,1}^z S_{k,2}^z + 2h_k S_k^z \tag{9}$$
$$H^{\rm D} = -2 \sum_{k,m=1,2} S_{k,m}^x \,.$$

We note that the inter-cell Hamiltonian $H_{1,2}^{\rm P}$ in Eq. (6) does not possess the qubit permutation symmetry. However, as explained above, the qubits in each cell tend to evolve as homogenous clusters. Therefore one can approximate the inter-cell Hamiltonian in terms of the total spin operators for the columns

$$H_{1,2}^P \simeq -\frac{8}{n} J S_{1,2}^z S_{2,2}^z \,. \tag{10}$$

We observe that the system Hamiltonian commutes with the total spin operators $S_{k,m}^2 = \sum_{\alpha\in x,y,z} (S_{k,m}^\alpha)^2$. Given that all qubits in the initial state are polarized along the x-axis this restricts the evolution to the subspace of maximum total spin values $n/4$ for each column. This subspace is spanned by the basis vectors $|n/4, m_{k,m}\rangle$ corresponding to the definite projections of column spins on the z axis $m_{k,m} = -n/4, \ldots, n/4$. As a measure of the error incurred by this approximation, it can be shown that the two lowest energy levels are within 0.1% of the exact values for the case of interest, $n = 8$.

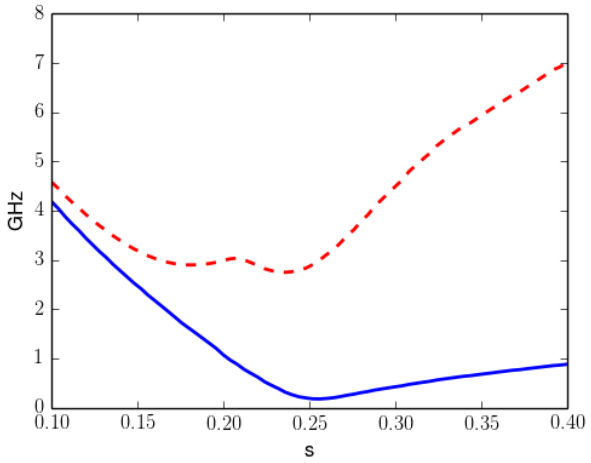

FIG. 3. Gap of the quantum Hamiltonian for $h_1 = 0.44$ as a function of the annealing parameter. The continuous line is the energy difference between the ground state and the first excited state. The avoided crossing at $s = 0.26$ corresponds to a minimum gap of 180 MHz. The dashed line is the energy difference between the ground state and the second excited state.

B. Effective energy potential the classical paths of product states

We now derive the effective potential over product states used to study the difference between thermal hoping among classical paths, and quantum tunneling in the quantum models. This will also serve to clarify the tunneling picture described above. We first transform to a representation that contains an explicit momentum operator. We think of each cluster k as a "particle" with the coordinate proportional to its total spin z projection $\sum_{j=1,2} S^z_{k,j}$. Because the x-component of the total spin of the cluster does not commute with the z-component it is naturally associated with the momentum that causes the particle to move. This allows us to think of the z-component of a large spin as a particle moving in a slowly time-varying potential, formalizing the cartoon pictures sometimes drawn to illustrate quantum annealing that show a particle escaping a local minimum in a continuous potential via tunneling.

The canonically conjugated coordinate and momenta operators can be naturally introduced within the WKB framework (see App. B)

$$S^z_{1,k} + S^z_{2,k} = \frac{n}{2} q_k \tag{11}$$

$$S^x_{1,k} + S^x_{2,k} \approx \frac{n}{2}\sqrt{1-q_k^2}\cos p_k \ . \tag{12}$$

where $[q,p] = i(2/n)$ and $2/n \ll 1$ plays a role of Planck constant in traditional WKB. To the leading order in $1/n$ the Hamiltonian becomes

$$H^{\rm WKB}(q_1,q_2,p_1,p_2,s) = -nA(s)\sum_{k=1,2}\sqrt{1-q_k^2}\cos p_k + nB(s)J\sum_{k=1,2}\Big(h_k\sum_j q_k - nq_k^2/4\Big) - \frac{n}{2}B(s)J\,q_1\,q_2 \ . \tag{13}$$

WKB theory based on this Hamiltonian describes eigenstates and eigenvalues with logarithmic accuracy in the asymptotic limit $n \gg 1$. It also gives a reasonable estimates already for $n = 8$ (see App. B).

We will now consider the potential corresponding to a low energy description with very low momentum

$$U(q_1,q_2,s) = H^{\rm WKB}(q_1,q_2,0,0,s) \ .$$

The same potential is obtained in Ref. [5] projecting the Hamiltonian of large spin operators Eqs. (9), (10) over spin coherent states, which are product states. The different panels in Figure 4 depict the potential $U(q_1,q_2)$ for different values of the annealing parameter s with local field $h_1 = 0.44$. Initially ($s = 0$) there is only a global minimum at $q_1 = q_2 = 0$ corresponding to all spins aligned with the x-direction. As s grows the minima begins to move to the left corner $(-1,1)$ corresponding to the opposite orientations of the clusters. This effect was already mentioned above in the general context. The terms in the effective potential corresponding to the local fields h_k are linear in q_k, and dominate the Ising coupling energy between the large spins that is is quadratic in q_k for $|q_k| \ll 1$. For larger values of s the Ising terms begin to compete with the local fields and the plateau is formed in the vicinity of $q_1 = 0$ following the local bifurcation of U and giving rise to a new minimum corresponding to the ferromagnetic alignment of the two clusters. At some value s_c the two minima coexists with the same energy. For $s > s_c$ the minimum corresponding to the ferromagnetic cluster alignment has a lower energy, smoothly connecting to the solution state at the end of quantum annealing corresponding to the global minimum of the potential $U(q_1,q_2,s=1)$ at $q_1 = q_1 = 1$.

In a closed system quantum adiabatic evolution algorithm the system tunnels from the old global minimum to the new one in the vicinity of s_c [5]. It tunnels under the barrier whose top approximately corresponds to zero z-magnetization $q_1 = 0$. The tunneling corresponds to the avoided crossing between the two lowest energy levels of the quantum Hamiltonian $H_0(s)$ of Eq. (1) shown in Fig. 3. During the tunneling the total spin of the left cluster switches its direction. The switching manifests itself in Fig. 5 as a steep change in s-dependence of the quantum mechanical average of the the left cluster polarization $\langle q_1\rangle$ in the instantaneous ground state. In contrast, the right cluster which does not tunnel displays a smooth behavior of its average polarization $\langle q_2\rangle$.

In classical dynamical evolutions, when tunneling is not possible, the system will continue to reside in the initially global minimum emanating from the point $(0,0)$. Fig. 6 shows the energies of the two classical

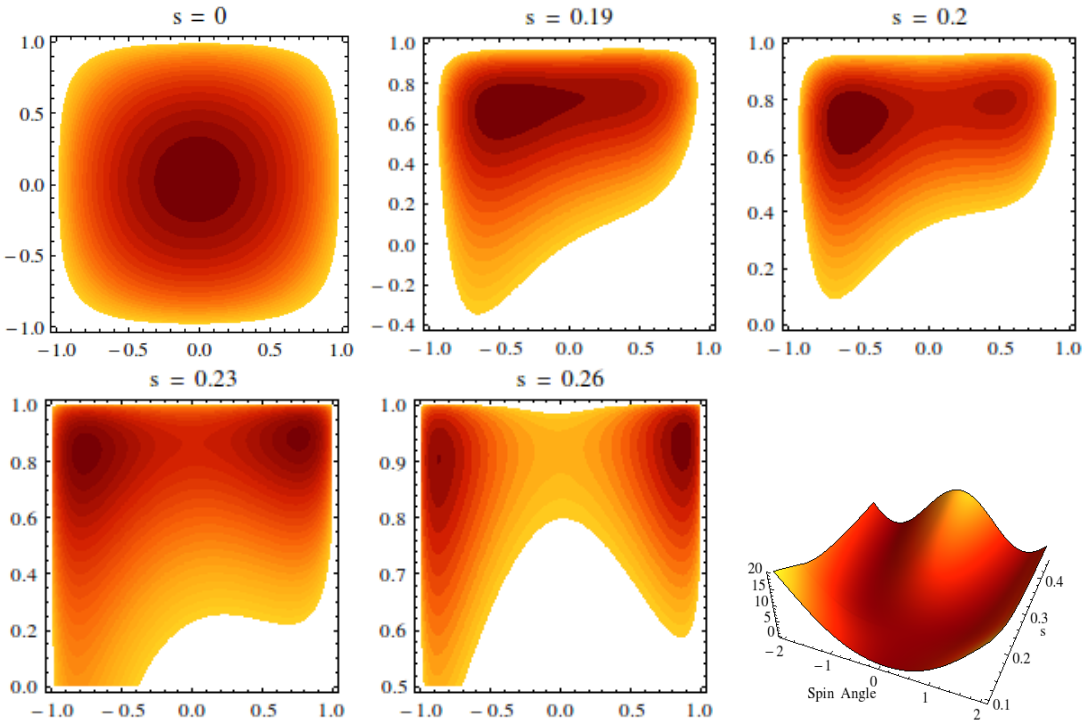

FIG. 4. The five snapshots in this figure show how the energy landscape evolves and a double-well potential is formed during annealing schedule. The 3D plot also depicts such evolution as a function of an effective orientation angle for the large spins. The minimum that forms first would trap a classical particle moving in this potential. Later in the annealing evolution a second minimum forms and eventually becomes the global minimum. To reach this global minimum the system state has to traverse the energy barrier between them. The origin of this bifurcation is explained in the text.

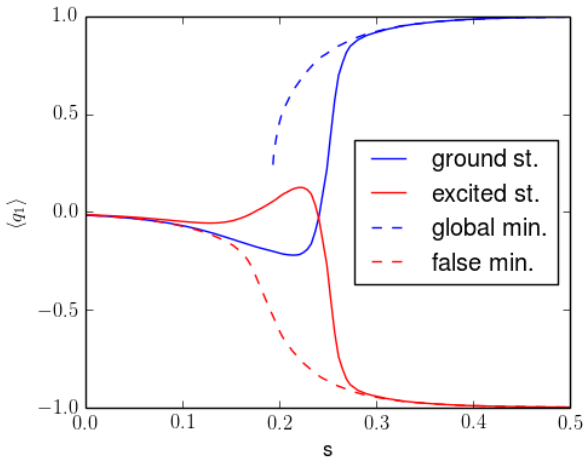

FIG. 5. Plot of $\langle q_1 \rangle$ for the quantum ground state and first excited state as a function of the annealing parameter s for $h_1 = 0.44$. We also plot the value of the parameter q_1 along the paths corresponding to the false and global minima for the effective energy potential. The correspondence is good, except at the avoided crossing where the quantum states are entangled.

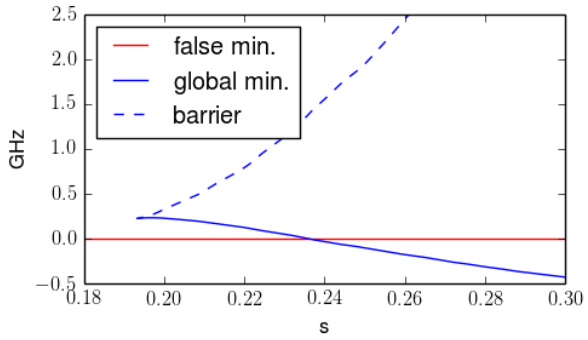

FIG. 6. Bifurcation for $h_1 = 0.44$. The energies of the paths of the double-well minima and the height of the effective energy barrier in GHz are plotted in GHz. We subtract the instantaneous energy of the final false minima. The path corresponding to the global minimum appears as a bifurcation with higher energy. When this path crosses with the path of the final false minimum, the height of the energy barrier is substantial.

paths corresponding to the two minima of the energy potential $U(q_1, q_2, s)$ for $h_1 = 0.44$. Classical dynamical evolutions will get trapped in the false minimum path due to the bifurcation seen in this figure. Classical trajectories can only reach the global minimum through thermal excitations. In Figure 5 we also show the value of the parameter q_1 corresponding to the local minima of $U(q_1, q_2, s)$ as a function of the annealing parameter s. The parameter q_1 for the classical path connecting to the final false minimum first aligns with the quantum ground state and later aligns with the quantum first excited state. This path starts at the point $(0, 0)$. The bifurcation path corresponding to the global minimum first appears with a definite but small q_1, and later aligns with the quantum

ground state after the avoided crossing.

III. MODELING THE ANNEALING DYNAMICS

A. Open quantum system models

Under realistic conditions, the performance of a quantum annealer as an optimizer can be strongly influenced by the coupling to the environment. In order to capture this effect we present a *phenomenological* open quantum system model by incorporating the experimental characterization of the noise that was performed to date on D-Wave devices (the experimental platform for the present investigation).

We shall assume that each flux qubit is coupled to its own environment with an independent noise source; this assumption is consistent with experimental data [8]. We separate the bath excitations into two parts. Excitations with frequencies slower than the annealing rate in our experiments (5 KHz) will be treated as a "static noise" whose effect can be included by an appropriate averaging of the success rate over the local field errors ($\sim 5\%$ for the D-Wave II chip). The excitations with higher frequencies will be modeled as a bath of harmonic oscillators. This approach is quite general, independent of the true physical source of the noise, being valid under the condition that the bath is in thermal equilibrium, can be treated within the conditions of linear response theory, and has Gaussian fluctuations [19]. The corresponding system-bath Hamiltonian is

$$H(s) = H_0(s) + \frac{1}{2}\sum_{\mu=1}^{2n} \sigma_\mu^z Q_\mu(s) + H_B, \quad s = t/t_{qa}. \tag{14}$$

Hereafter we will use for brevity a single index μ for single-qubit Pauli matrices instead of the double indexation employed in Sec. II. In the equation above, t_{qa} is the duration of the quantum annealing process, $H_0(t)$ is the Hamiltonian for an N-qubit system (as in Eq. 1), H_B is the standard Hamiltonian of the bosonic bath, and $Q_\mu(s)$ is a bosonic noise operator that couples the μ^{th} qubit to its environment. The coupling parameters of bosonic bath operator $Q_\mu(s)$ depend on the annealing parameter s through the persistent current (see App. A). In what follows we use the notation Q_μ and make the dependence on s implicit for simplicity.

The properties of the system's noise are determined by the noise spectral density $S(\omega)$:

$$\int_0^\infty e^{i\omega t}\langle e^{iH_B t} Q_\mu e^{-iH_B t} Q_\nu\rangle = S(\omega)\delta_{\mu\nu}, \tag{15}$$

where the inclusion of the Kronecker delta function $\delta_{\mu\nu}$ is a consequence of the assumption of independent baths. The temperature dependence of the spectral density is given by

$$S(\omega) = \hbar^2 J(\omega)(\bar{n}(\omega)+1)\,, \tag{16}$$

where $n(\omega) = [\exp(\beta\omega)-1]^{-1}$ is the Planck number at temperature $T = \hbar/k_B\beta$ and $J(\omega)$ is the temperature-independent spectral function [20] that can be treated as an antisymmetric function of frequency, $J(\omega) = [S(\omega) - S(-\omega)]/\hbar^2$.

The effect of the Ohmic noise on multiqubit quantum annealing was studied numerically in [21]. This work assumed weak system-environment coupling and utilized the Redfield formalism to derive the quantum Markovian master equation in the basis of the (instantaneous) adiabatic eigenstates of the qubit Hamiltonian. It was built on earlier studies of open-system quantum annealing in [22–26] where similar assumptions were made.

In addition to Ohmic noise, an important role is played by a low-frequency noise of the $1/f$ type [27, 28] produced by the spins in the amorphous parts of the qubit device [12, 14, 29]. In current D-Wave chips this noise is coupled to the flux qubit relatively strongly as was shown in recent experiments [17]. Additionally, our analysis shows that noise effects are significantly enhanced by collective effects associated with multiqubit cotunneling. While future generations of quantum annealer chips will hopefully have reduced levels of flux qubit noise, it will still produce a highly nonlinear effect for sufficiently a large number of cotunneling qubits.

In recent years, the noise spectrum of flux qubits was studied using a variety of approaches that includes dynamical decoupling schemes [30], free-induction Ramsey interference [31], coherent spectroscopy with strong microwave driving [32], and macroscopic resonant tunneling (MRT) techniques [17, 33].

In MRT experiments the qubit state is probed in a way that is most similar (compared with other methods) to the quantum annealing process itself, without using high-frequency driving and involving slow tunneling dynamics of each qubit within its ground-state manifold. While the exact microscopic models of low-frequency noise are not well understood [12, 14] its effect on system evolution in MRT experiments appeared to be well described by phenomenological models [17, 33]. There, the quantity of interest is the incoherent-tunneling rate between the "up" and "down" eigenstates of the single flux qubit Hamiltonian $-\frac{1}{2}(\epsilon\sigma^z + \Delta\sigma^x)$ as a function of the bias ϵ. In [34], the Gaussian form of the MRT line is described with a noise model whose spectral density is sharply peaked at low frequency. In [17], this model is extended by attributing the linear form of the tails in the MRT line shape to the high-frequency (Ohmic) part of the noise spectral density. The MRT data collected for small tunneling amplitudes ($\Delta < 1$ MHz) and in a broad range of frequencies (0.4MHz $-$ 4 GHz) and temperatures (21 mK $-$ 38mK) are surprisingly well described by a phenomenological "hybrid" noise model

$$S(\omega) = S_{LF}(\omega) + S_{HF}(\omega), \tag{17}$$

where the high-frequency part of the noise has a standard Ohmic form, [35]

$$J_{HF}(\omega) = \eta\omega\exp(\omega/\omega_c), \tag{18}$$

and the low-frequency part is described only by its

first two cumulants related to the width W and shift ϵ_p of the MRT line:

$$W^2 = \int_0^\infty \frac{d\omega}{2\pi} J_{LF}(\omega) \coth \frac{\hbar\omega}{k_B T}, \tag{19}$$

$$\epsilon_p = \int_0^\infty \frac{d\omega}{2\pi} \frac{J_{LF}(\omega)}{\omega} \tag{20}$$

often called the reorganization energy, i.e. the energy change of the bath degrees of freedom during an incoherent tunneling process. The width W and shift ϵ_p measured in [17] satisfy the thermodynamic relation $W^2 = \frac{2k_B T}{\hbar}\epsilon_p$ which requires that the characteristic cutoff of the low-frequency noise, $\omega_{FL} \ll k_B T/\hbar$. The hybrid model uses no information about the noise spectrum at frequencies below W except the assumption that $\hbar\omega_{LF} \ll W$. It is justified because in the experiments $W \sim K_B T$ [17].

The noise linewidth $W = W(s)$, as probed by a qubit, depends on the point at which it is taken the annealling process via a persistent current. In our study we will use the data from [17] collected on a D-Wave I device. Similar measurements done in the D-Wave II chip used here yield similar parameters.

During the quantum annealing the system typically follows several stages identified in [21] depending on the magnitude of the instantaneous energy gap between the ground-state energy $E_0(s)$ and the excited-state energy $E_1(s)$ of the control Hamiltonian $H_0(s)$, whose energy spectrum evolves during quantum annealing according to

$$H_0(s)|\psi_\gamma(s)\rangle = E_\gamma(s)|\psi_\gamma(s)\rangle. \tag{21}$$

In the problem studied here with two coupled clusters, the separation between the ground state to the second excited state (> 3GHz) is much greater than the temperature during the entire course of the quantum annealing. Therefore the dynamics of the $2n$ qubit system can be described using the two lowest-energy instantaneous eigenstates $\{|\psi_0(s)\rangle, |\psi_1(s)\rangle\}$.

At the beginning of quantum annealing, the qubit Hamiltonian H_0 (as in Eq. 1) is dominated by the driver Hamiltonian term and the energy gap between the ground state and the first excited state ($\simeq 2A(s) \sim 5$GHz) is very large compared to the temperature. At that stage the system resides in a ground state $|\psi_0(s)\rangle$ with overwhelming probability. For local fields $h_1 < J/2$, the system evolution goes through the so-called "avoided-crossing" region at intermediate times where $E_1(s)$ and $E_0(s)$ approach closely to, and then repel from, each other. (See inset in Fig. 3.) This level repulsion occurs due to the cotunneling of qubits in the left cluster between the opposite z-polarizations. At the point where the gap $E_1(s) - E_0(s)$ reaches its minimum $\Delta E_{\min}$ the corresponding adiabatic eigenstates are formed by the symmetric and anti-symmetric superpositions of the cluster orientations (cf. Fig. 7).

The success of closed-system quantum annealing is limited by the Landau-Zener transitions away from the adiabatic group state whose probability decreases exponentially with the ratio $\Delta E_{\min}^2/v_{qa}$ of the square of minimum energy gap to the quantum annealing rate v_{qa}. In our experiments, the quantum annealing rate is 50 kHz and the error due to Landau-Zener transitions is very small; it is 1% for the smallest gap in our study of approximately 5MHz achieved at $h_1/J = 0.48$, and it becomes completely negligible for smaller values of h_1/J (e.g. 10^{-10} for $h_1/J = 0.46$). The minimum gap is less than the temperature, $\Delta E_{\min} \lesssim k_B T$, for most of the h_1/J values under study (cf. Fig. 7). Therefore the population of the excited state at the end of quantum annealing is entirely due to thermal excitation [15, 16, 36].

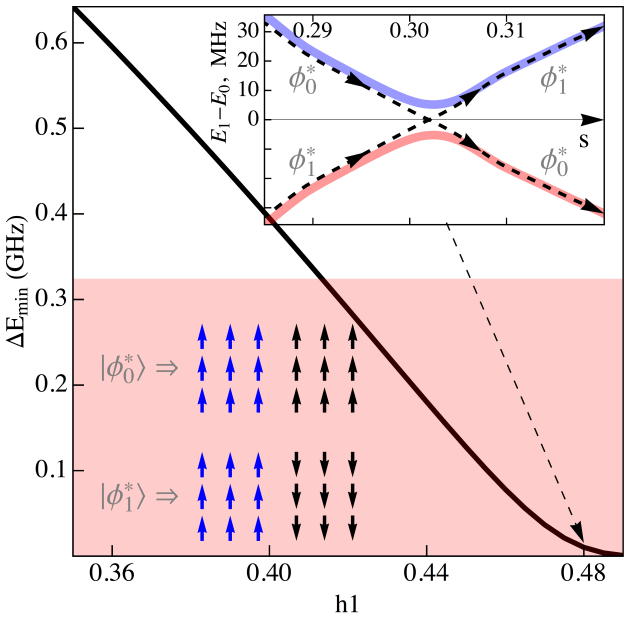

FIG. 7. The minimum gap between the ground- and first excited-state levels $\Delta E_{min} = \min_{s\in(0,1)}[E_1(s) - E_0(s)]$ (21) during quantum annealing as a function of the rescaled bias h_1/J is shown by the solid green line. The horizontal boundary of the red-filled area at 324MHz corresponds to 15.5mK, which is the lowest temperature in our experiments. The bias value $h_1/J = 0.5$ corresponds to zero energy gap, which is achieved at the end of quantum annealing when the eigenstates of $H_0(t_{qa}) = H_P$ with parallel and anti-parallel cluster orientations are degenerate. The upper inset shows the avoided crossing between the energy levels $E_1(s)$, $E_0(s)$ in the weak-strong cluster problem at $h_1/J = 0.48$. Dashed lines show the energy levels corresponding to the diabatic basis of states $|\phi_1^*(s)\rangle, |\phi_i^*(s)\rangle$ (29) formed by the rotation of the adiabatic eigenstates (21) that maximizes the average Hamming distance (25), (28) between the spin configurations. The lower inset shows the spin configurations in both clusters that dominate the characteristics of the eigenstates before and after the avoided crossing. During the passage of the avoided crossing, spins in the left cluster (shown in black) reverse their orientations.

When the instantaneous energy gap $E_1(s) - E_0(s)$ is sufficiently large compare to $W(s)$, the coupling to environment can be treated as a perturbation. This regime corresponds to the initial stage of evolution up to approximately the avoided crossing. In the perturbative regime, the transition rate between the first excited state and a ground state of the control Hamiltonian $H_0(s)$ is given by Fermi's golden rule for a

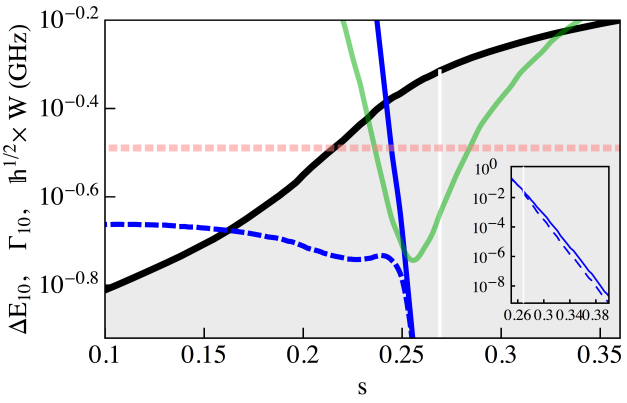

FIG. 8. The solid black line shows the dependence of the effective linewidth of the low-frequency noise $\hbar^{1/2}(s)W(s)$ on annealing parameter s. The dashed blue line is a plot of the transition rate (57) Γ_{10}^{FGR} vs. s calculated in second order in spin-boson interaction using Fermi's golden rule (22). The solid blue is a plot of the transition rate Γ_{10} calculated using NIBA (57). The green line shows the s-dependence of the energy gap $E_1(s)-E_0(s)$ between the two lowest-energy levels during the annealing at 15.5 mK. The lowest temperature in our experiments is shown by the horizontal red dotted line. All plots correspond to bias $h_1 = 0.44J$. At the early stage of quantum annealing $\hbar^{1/2}(s)W(s) \ll E_1(s)-E_0(s)$ and Γ_{10}^{FGR} gives an accurate description of the dynamics. The inset show the transition rates Γ_{10}^{FGR}, Γ_{10} vs. s using the same units as in the main plot but showing a greater range of values. Vertical white lines in the inset and main plot mark the value of $s_{eq} = 0.269$ where the deviation of the system state from instantaneous Gibbs distribution is 1%. This deviation grows very rapidly for greater values of s due to the suppression of the transition rates (cf. Fig. 9). Only the stage of the quantum annealing with $s \gtrsim s_{eq}$ determines the final ground state population. One can see that at that stage $\hbar^{1/2}(s)W(s) \gg \Gamma_{10}$, justifying the NIBA approximation discussed in the main text.

single-boson process:

$$\Gamma_{10}^{\rm FGR}(s) = \mathbb{b}(s)J(\omega_{10})[\bar{n}(\omega_{10})+1], \qquad (22)$$

where $\omega_{10} = (E_1(s)-E_0(s))/\hbar$ is the Bohr frequency for the transition and

$$\mathbb{b}(s) = \frac{1}{4}\sum_{\mu=1}^{2n}|Z_\mu^{10}(s)|^2. \qquad (23)$$

Here and below we use the following notation for the matrix elements:

$$Z_\mu^{\gamma\gamma'}(s) = \langle\psi_\gamma(s)|\sigma_\mu^z|\psi_{\gamma'}(s)\rangle, \quad \gamma,\gamma' = 0,1. \qquad (24)$$

This is an overlap factor that determines how strongly the transition $1 \leftrightarrow 0$ is coupled to the environment. Fig. 9 shows the dependence of $\mathbb{b}(s)$ on the annealing parameter s. We observe a steep exponential fall-off off this coefficient after the avoided crossing. This happens because, starting from the avoided crossing region, intra-cell ferromagnetic interaction plays a substantial role by causing the spins in each unit cell to move *in unison*, forming two clusters with total spin value $n/2$ each. As can be seen from Fig. 5, the first two eigenstates $|\psi_0\rangle$ and $|\psi_1\rangle$ after the avoided

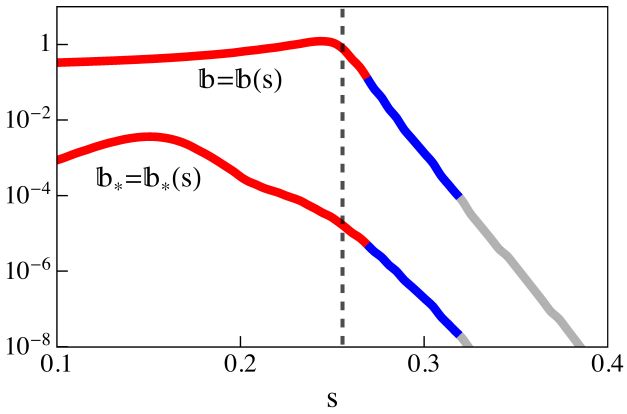

FIG. 9. Dependence of the overlap factor $\mathbb{b}$ on s for $h_1 = 0.44J$. The two plots correspond to the overlap coefficient in the adiabatic basis $\{|\psi_0\rangle, |\psi_1\rangle\}$ and rotated (diabatic) basis (29). Vertical dashed line indicates the point where the minimum energy gap is reached (avoided-crossing). Red, blue, and gray colors indicate the different stages of the quantum annealing described in the text.

crossing correspond to opposite total spin z- projections of the left cluster. When s increases, the average "Hamming distance" between the eigenstates,

$$\mathbb{h}(s) = \frac{1}{4}\sum_{\mu=1}^{2n}|Z_\mu^{11}(s) - Z_\mu^{00}(s)|^2, \qquad (25)$$

also increases very steeply as shown in Fig. 10. (We note that the maximum value of $\mathbb{h}(s)$ is proportional to n.) In that region the transition between the eigenstates requires qubit cotunneling of a progressively higher order, leading to an exponential decay of the overlap coefficient $\mathbb{b}(s)$ with s and a steep deceleration of the environment-induced transitions between the two states, as can be seen from the plot of $\Gamma_{10}^{\rm FGR}(s)$ in Fig. 8.

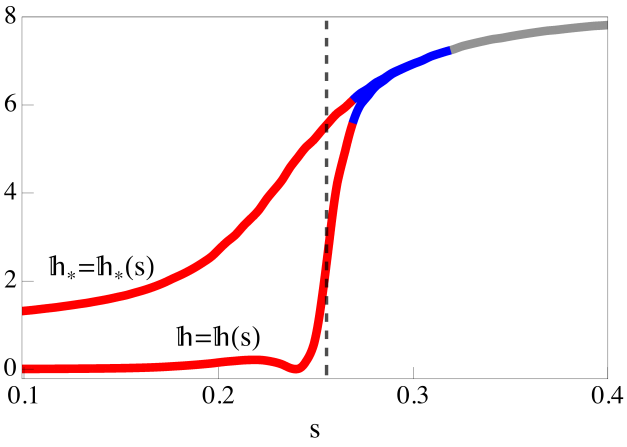

FIG. 10. Dependence of the average Hamming distance between the two lowest-energy eigenstates on s for adiabatic basis $(|\psi_0\rangle, |\psi_1\rangle)$ and rotated diabatic basis (29) for $h_1 = 0.44J$. The vertical dashed line indicates the point where the minimum energy gap is reached (avoided-crossing). Red, blue, and gray colors indicate the different stages of the quantum annealing described in the text.

The fact that qubits within each unit cell tend to

move together, forming large spins, amplifies the effect of the environment on their quantum dynamics. In particular, we will show below that the effective linewidth of the low-frequency noise as seen by the two-state system $\{|\psi_1(s)\rangle, |\psi_0(s)\rangle\}$ system is $\mathbb{h}^{1/2}(s)W(s)$ and that the effective Ohmic coefficient is $\mathbb{h}(s)\eta(s)$. This amplification becomes important when clusters increase their z-polarizations and $\mathbb{h} \sim n >> 1$ (see Fig. 8) at later stages of the quantum annealing. For sufficiently large $\mathbb{h}^{1/2}(s)W(s) \gtrsim \Delta E_{\min}$, the description of the system dynamics becomes substantially non-perturbative in the spin-boson interaction. Equilibria of the environmental degrees of freedom shift depending on the collective qubit-state evolution, which in turn affects the state itself causing the *polaronic* effect. In this case, the adiabatic basis of instantaneous eigenstates $\{|\psi_1(s)\rangle, |\psi_0(s)\rangle\}$ formed by the superposition of up and down cluster orientations loses its physical significance. Instead, the dynamics occurs between the two *diabatic* states $\{|\phi_1(s)\rangle, |\phi_0(s)\rangle\}$ with the predominately opposite cluster orientations corresponding (roughly) to the bottoms of the wells of the classical potential in Fig. 4 separated by the barrier.

We introduce a unitary rotation on angle ϑ defining a new basis of states $|\phi_{0,1}(\vartheta, s)\rangle$:

$$|\phi_i\rangle = \sum_{j=0,1} (-1)^{ij+j+1} \cos\left(\frac{\vartheta}{2} - (-1)^{i+j}\frac{\pi}{4}\right)|\psi_j\rangle, \tag{26}$$

where $i, j = 0, 1$, and corresponding matrix elements

$$Z_\mu^{\gamma\gamma'}(\vartheta, s) = \langle\phi_\gamma(\vartheta, s)|\sigma_\mu^z|\phi_{\gamma'}(\vartheta, s)\rangle, \quad \gamma, \gamma' = 0, 1. \tag{27}$$

We find the angle $\vartheta_*(s)$ that maximizes the average Hamming distance between the states

$$\mathbb{h}_*(s) = \max_\vartheta \frac{1}{4}\sum_{\mu=1}^{2n} |Z_\mu^{11}(\vartheta, s) - Z_\mu^{00}(\vartheta, s)|^2. \tag{28}$$

Then our new instantaneous basis will be

$$|\phi_\gamma^*(s)\rangle = |\phi_i(\vartheta_*(s), s)\rangle, \quad \gamma = 0, 1. \tag{29}$$

The system dynamics is mostly a hopping between these states associated with the incoherent cotunneling of the spins in the left cluster connecting states with predominantly "up" ($|\phi_1^*\rangle$) and "down" ($|ket\phi_0^*$) qubit configurations that are in average a Hamming distance $\mathbb{h}_*(s)$ apart. ($\mathbb{h}_*(s)$ is shown in Fig.10.) In essence, this approach is related to the pointer basis idea, that the system tends to be localized in states induced by environmental coupling [37].

The rotation angle $\vartheta^*(s)$ during the annealing is shown in Fig.11 for different vales of h_1/J. In the later stages of the annealing the angle ϑ always approaches the value $\pi/2$ that corresponds to the adiabatic (energy) basis with state $|\phi_1^*\rangle$ being an excited state 26. In other words, quantum annealing along the pointer states arrives at the encoded solution of the computational problem because toward the end of the annealing the pointer basis converges back to eigenstates of the problem Hamiltonian.

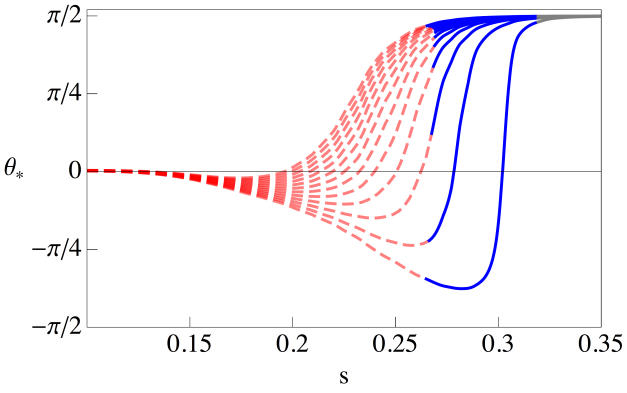

FIG. 11. Optimal rotation angles ϑ^* vs. s for diabatic eigenstates (29) at different values of $h_1/J = 0.35 + 0.01i$, with $i = 1, 2, \ldots, 13$ corresponding to the curves in the figure numbered from the bottom to the top. Red corresponds to the thermalization phase, blue corresponds to the loss of thermalization, and black corresponds to the frozen phase described in the main text. Optimal rotation angles only have physical meaning starting from about the end of the thermalization phase where the spins in the cells start to behave in a concerted manner. All angles approach $\pi/2$ in a frozen phase corresponding to the adiabatic eigenstates.

We will show below that the non-perturbative treatment of the effects of noise and dissipation does not change the Markovian nature of the system dynamics but modifies the instantaneous transition rate $\Gamma_{10}(s)$ compared to its value $\Gamma_{10}^{FGR}(s)$ (22) from a single-boson process. The non-perturbative analysis in the rotated basis is justified within the context of the theory of spin-boson interaction developed in [35]. The individual transitions due to the coupling to bosons are associated with so-called "blip-cojourn" pairs with blips forming a dilute gas if the duration of the blip $\tau_b = 1/\mathbb{h}^{1/2}(s)W(s)$ is much shorter than the characteristic inter-blip distance $\sim 1/\Gamma_{10}(s)$, with

$$\Gamma_{10}(s) \ll \mathbb{h}^{1/2}(s)W(s). \tag{30}$$

In the adiabatic basis, $\mathbb{h}(s)$ can reach very small values near the avoided crossing (see Fig.10) due to the spurious quantum interference effects. In the optimally rotated (diabatic) basis, $\tau_b^{-1} = (\mathbb{h}^*(s))^{1/2}W(s)$ is monotonically increasing during the annealing to its maximum value (n=8 in the problem of interest). When the condition (30) is satisfied at the last stages of the annealing, the gas of blips is dilute and we can apply the Noninteracting-blip Approximation (NIBA) [35]. While this method was applied to analyze a Landau-Zener problem in a driven spin-1/2 system coupled to a finite temperature bath in a number of papers [15, 16, 38], its application in the present context of strongly correlated qubit dynamics is novel and leads to qualitatively different features.

Before we proceed further with NIBA analysis, we emphasize that our theory will not provide an accurate treatment of the region of s where $\mathbb{h}^{1/2}(s)W(s) \sim \Gamma_{10}$, representing a crossover between the perturbative treatment based on single-boson processes and Ohmic spectral density ($\Gamma_{10}^{FGR}(s)$) and non-perturbative NIBA theory that includes low-frequency

noise ($\Gamma_{10}(s)$). In this intermediate region the low-frequency noise cannot be described by the two lowest cumulants of its special density and we are simply lucking the experimental data for the theoretical analysis.

Our main observation is that this region does not affect the population of the ground state at the end of the quantum annealing. Since the quantum annealing rate $1/t_{qa}$=50 kHz is constant, the system stays very close to an instantaneous thermal equilibrium while

$$\Gamma_{10}^{\rm FGR}(s),\, \Gamma_{10} \gg 1/t_{qa} \tag{31}$$

(see Fig. 8). This is a "thermalization phase" of the annealing process. On the other hand, due to the strong effect of low-frequency noise on D-Wave qubits the condition

$$1/t_{qa} \ll \hbar^{1/2}(s) W(s) \tag{32}$$

is held almost everywhere except for the very early stages (cf. Fig. 8). Therefore the non-perturbative regime (30) is established well within the thermalization phase where the (Gibbs) distribution function is not sensitive to the noise model.

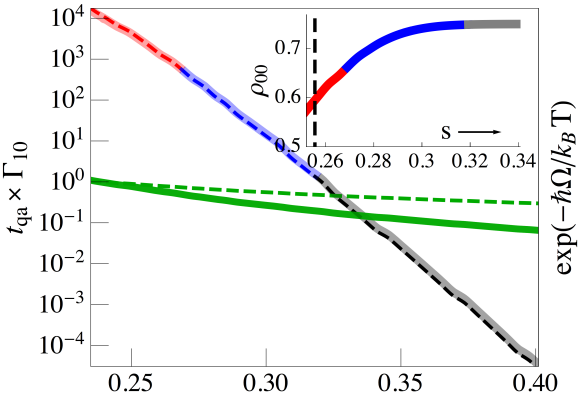

FIG. 12. In main plot, the solid line with red, blue, and black coloring shows the dependence of $t_{qa}\,\Gamma_{10}$ (57) on the annealing parameter s. Red corresponds to the thermalization phase, blue corresponds to the loss of thermalization, and black corresponds to the frozen phase described in the main text. The solid green line is a plot of the Gibbs factor for the instantaneous energy difference $\hbar\Omega(s)$ between the diabatic states given in (37). Both lines are plotted at 15.5mK. Dashed lines correspond to the temperature 35mK. The inset shows the evolution of the instantaneous population of the diabatic eigenstate $\langle\phi_0^*(s)|\rho|\phi_0^*\rangle$. The colors correspond to the same stages of quantum annealing as in the main plot. All data are for the value of the local field $h_1/J = 0.44$.

At a later stage the thermal distribution can no longer be supported due to the steep slowdown of the transition rates as shown in Fig. (12). Then the system enters the final "frozen" stage where the transitions are suppressed over the period of the annealing and part of the system population remains trapped in the excited state. As can be seen in the insert of Fig. 12, the success probability is determined by the occupation of the ground state at the beginning of the frozen phase determined by the Gibbs factor $\exp(-(E_1-E_0)/k_BT)$. When the temperature grows, the transition rates dominated by low-frequency noise change very little, while the Gibbs factor increases appreciably as can be seen from Fig. (12). This in turn increases the population of the excited state, reducing the success of the quantum annealing as will be seen later.

B. Non Interacting Blip Approximation

To implement NIBA in our problem we need to explicitly represent the environmental degrees of the boson operators that diagonalize the free-boson Hamiltonian $H_B = \sum_{\mu=1}^{2n}\sum_\nu \hbar\omega_{\mu\nu}(b_{\mu\,\nu}^\dagger b_{\mu\nu} + 1/2)$:

$$Q_\mu = \sum_\nu \lambda_{\mu\nu}(b_{\mu\,\nu}^\dagger + b_{\mu\nu}), \quad \mu = 1,\ldots,2n. \tag{33}$$

Here $\lambda_{\mu\nu}$ and $\omega_{\mu\nu}$ are the microscopic parameters that will not enter into any observable directly but will do so only via the spectral function (16) $J(\omega) = 2\pi\sum_\mu(\lambda_{\mu\nu}/\hbar\omega_{\mu\nu})^2\delta(\omega-\omega_{\mu\nu})$, identical for each qubit. We proceed by making a small polaron transformation of the original Hamiltonian with unitary operator

$$U(s) = \exp\left[\sum_\gamma -\Lambda_\gamma(s)|\phi_\gamma^*(s)\rangle\langle\phi_\gamma^*(s)|\right]$$

. Here we use the notation

$$\Lambda_\gamma(s) = \sum_{\mu\nu}\xi_{\mu\nu}^{\gamma\gamma}(b_{\mu\nu}-b_{\mu\nu}^\dagger), \quad \xi_{\mu\nu}^{\gamma\gamma'} = \frac{\lambda_{\mu\nu}}{\hbar\omega_{\mu\nu}} Z_\mu^{\gamma\gamma'}, \tag{34}$$

where the indexes μ,ν and γ run over their respective ranges defined above and matrix elements $Z_\mu^{\gamma\gamma'}$ are defined in the diabatic basis as

$$Z_\mu^{\gamma\gamma'}(s) = \langle\phi_\gamma^*(s)|\sigma_\mu^z|\phi_{\gamma'}^*(s)\rangle. \tag{35}$$

The system Hamiltonian after the transformation $\mathbb{H}_0 = UH_0U^{-1}$ can be written (up to identity operator) as

$$\mathbb{H}_0 = \hbar\Omega\left(|\phi_1^*\rangle\langle\phi_1^*| - |\phi_0^*\rangle\langle\phi_0^*|\right), \tag{36}$$

where

$$\Omega(s) = \varepsilon(s)\sin\vartheta_*(s) - \hbar\epsilon_p\mathbb{d}(s) \tag{37}$$

and $\varepsilon = (E_1 - E_0)/\hbar$. The first term above corresponds to the system energy gap in a diabatic (pointer) basis and the second term gives the polaronic shift due to reorganization energy of the environment. Similar to the linewidth, it is renormalized with respect to its single qubit MRT value by a coefficient $\mathbb{d}(s)$ reflective of a collective qubit behavior:

$$\mathbb{d} = \frac{1}{4}\sum_{\mu=1}^{2n}\left[(Z_\mu^{11})^2 - (Z_\mu^{00})^2\right]. \tag{38}$$

The Hamiltonian of the coupling to environment after the polaron transform $\mathbb{H}_{int} = \mathbb{H}_{int}^{10}|\phi_1^*\rangle\langle\phi_0^*| + \text{h.c.}$ is strictly non-diagonal in the basis states and

$$\mathbb{H}_{int}^{\gamma\gamma'} = \left(\frac{\hbar\Delta}{2} + \sum_{\mu,\nu} Z_\mu^{\gamma\gamma'}\lambda_{\mu\nu}(b_{\mu\nu}^\dagger + b_{\mu\nu} - 2\xi_{\mu\nu}^{\gamma\gamma'})\right) e^{\Lambda_{\gamma'\gamma}}, \tag{39}$$

where $\Lambda_{\gamma'\gamma} = \Lambda_{\gamma'} - \Lambda_\gamma$ and Δ represent off-diagonal element in the diabatic basis

$$\Delta(s) = -\epsilon(s)\cos\vartheta_*(s). \tag{40}$$

While original NIBA calculation [35] was quite involved, a very simple prescription for how to apply it was given in [39], which we will follow below. We start from the quantum Liouville equation for the full system-bath density operator $\varrho(s)$:

$$i\hbar\frac{d\varrho}{dt} = [\mathbb{H}_0 + \bar{\mathbb{H}}_{int}, \varrho(t)], \tag{41}$$

where we employed the interaction picture for bosons $\bar{\mathbb{H}}_{int}(t) = \exp(iH_Bt/\hbar)\mathbb{H}_{int}(t)\exp(-iH_Bt/\hbar)$. We write the density matrix in the pointer basis $\{|\phi^*_\gamma\rangle\}$ and express its non-diagonal matrix elements through diagonal ones as

$$\varrho_{10}(t) = \varrho_{10}(0) + \frac{1}{i\hbar}\int_0^t d\tau \exp\left(\frac{i}{\hbar}\int_\tau^t \Omega(\tau')\right) \times \left[\bar{\mathbb{H}}^{21}_{int}(\tau)\varrho_{11}(\tau) - \varrho_{22}(\tau)\bar{\mathbb{H}}^{21}_{int}(\tau)\right], \tag{42}$$

where for simplicity we used a physical time $t = t_{qa}s$. Here we made our *first approximation* and neglected the basis dragging terms $\langle\phi_1(s)|\dot{\phi}_0(s)\rangle$, because, as mentioned above, we focus on the situation where LZ transitions are negligible. Other than that the expression above is *exact*.

As a next step we use the fact that the initial state for quantum annealing corresponds to $\varrho_{10}(0) = 0$. We then plug the non-diagonal matrix elements from (42) back into (41) and obtain the equations for the diagonal matrix element

$$\frac{d\varrho_{11}}{dt} = -\frac{1}{\hbar^2}\int_0^t d\tau \exp\left(\frac{i}{\hbar}\int_\tau^t \Omega(\tau')\right) \times \left[\bar{\mathbb{H}}^{10}_{int}(t)\bar{\mathbb{H}}^{01}_{int}(\tau)\varrho_{11}(\tau) - \bar{\mathbb{H}}^{10}_{int}(t)\varrho_{00}(\tau)\bar{\mathbb{H}}^{01}_{int}(\tau)\right] + \text{h.c.} \tag{43}$$

and a similar equation for ϱ_{00}.

Our second approximation is to insert a free-bath dynamics into the expressions for $H^{\gamma\gamma'}_{int}(t)$ by replacing time-dependent boson operators $b_{\mu\nu}(t)$ with $b_{\mu\nu}(t)e^{-i\omega_{\mu\nu}t}$. Our third approximation is to introduce the decoupling anstatz for the full density matrix: $\varrho = \rho\otimes\rho_B$, where ρ_B is the Gibbs density operator for the bath and $\rho = Tr_B[\varrho]$ is the reduced density matrix of the qubit system. After that, the final step is to average (43) with respect to the bath, which can be done in a tedious but straightforward manner since averaging involves only free-boson operators. We write the resulting equation of the difference in populations of the pointer states $z(t) = \rho_{11}(t) - \rho_{00}(t)$ as

$$\frac{dz(t)}{ds} = \int_0^t dt'[h(t-t',s) - z(t')g(t-t',s)], \tag{44}$$

where $s = t/t_{qa}$ and functions h and g are

$$h(\tau,s) = 2Re[e^{i\Omega(s)\tau}(C(\tau - i\beta, s) - C(\tau,s)) \text{ and} \tag{45}$$

$$g(\tau,s) = 2Re[e^{i\Omega(s)\tau}(C(\tau - i\beta, s) + C(\tau,s)). \tag{46}$$

Here we used an inverse scaled temperature $\beta = \hbar/k_BT$.

The function $C(\tau,s)$ in the expressions above is the central result of our analysis as it is distinct from the conventional NIBA theory (cf. Eqs. (7.5),(7.6) in [35]). It has the following form

$$C(\tau,s) = F(\tau,s)\, e^{-\mathbb{h}_*(s)f(\tau,s)}, \tag{47}$$

where

$$F(\tau,s) = \mathbb{b}_*(s)f_{\tau\tau}(\tau,s) + (\epsilon_p\, \mathbb{c}_+(s) - i\mathbb{c}_-(s)f_\tau(\tau,s) - \Delta(s)/2)^2. \tag{48}$$

Here, the off-diagonal matrix element $\Delta(s)$ is given in (40) and we denoted $f_{\tau\tau} = \partial^2 f/\partial\tau^2$. We also used average Hamming distance (28) and the overlap factor $\mathbb{b}(s)$ (23) calculated in the diabatic basis using matrix elements from Eq. (35). The function $f(\tau,s)$ is related to the spectral density $S(s,\omega)$ and appears in the context of the MRT theory of flux qubits [17, 34] and Marcus theory [40]:

$$f(\tau,s) = \int_{-\infty}^{\infty}\frac{d\omega}{2\pi}S(\omega,s)\frac{1-e^{-i\omega t}}{(\hbar\omega)^2}. \tag{49}$$

Coefficients $\mathbb{c}_\pm(s)$ above have the form

$$\mathbb{c}_\pm(s) = \frac{1}{4}\sum_{\mu=1}^{2n} Z^{21}_\mu(s)(Z^{22}_\mu(s) \pm Z^{11}_\mu(s)), \tag{50}$$

where matrix elements Z are defined in the diabatic basis (35). Using the hybrid model of noise (17) introduced in [17] the function $f(\tau,s)$ takes the form

$$f(\tau,s) = i\epsilon_p(s)\tau + \frac{1}{2}W^2(s)\tau^2 - \frac{\eta}{2\pi}\ln G(\tau). \tag{51}$$

Here the function $G(\tau)$ is closely related to the well-known functions $Q_1(\tau), Q_2(\tau)$ discussed in Ref.[35] for the case of an Ohmic environment. Its explicit form is

$$G(\tau) = e^{-i\tan^{-1}(\tau\omega_c)}\sqrt{1+(\omega_c\tau)^2}, \times \frac{\Gamma((1-i\tau\omega_c)/\beta\omega_c)\Gamma((1+i\tau\omega_c)/\beta\omega_c)}{\Gamma^2(1/\beta\omega_c)} \tag{52}$$

where $\Gamma(x)$ is the Gamma function.

If follows from (47) and (49) that the functions $g(\tau,s)$ and $h(\tau,s)$ decay exponentially with τ on the scale $\tau_b = 1/(\mathbb{h}^{1/2}W(s))$ in correspondence with the discussion above. We observe that the population difference $z(t)$ in (44) varies on two distinct scales $t_{qa} >> \tau_b$. We first neglect the slow variation of $z(t)$ and calculate it locally at a given value of the quantum annealing parameter s. In this case the integral in (44) represents a simple convolution and the answer is given by the Laplace transform (similarly to [35]):

$$z(t|s) = \frac{1}{2\pi i}\int_{\mathcal{C}} d\lambda\, e^{\lambda t}\frac{\tilde{h}(\lambda) + \lambda z(0,s)}{\lambda(\lambda + \tilde{g}(\lambda))}, \tag{53}$$

where integration is done over the standard Bromwich contour $\mathcal{C}$. Here we explicitly introduced the parameter s in z to emphasize that all calculations are

performed at fixed s. We now suppose (following [35]) that $\tilde{h}(\lambda)$ and $\tilde{g}(\lambda)$ have well-defined expansions about zero (an assumption that will be validated self-consistently below):

$$\tilde{h}(\lambda) \simeq h_0 + \lambda h_1, \quad \tilde{g}(\lambda) \simeq g_0 + \lambda g_1. \tag{54}$$

Plugging this into (53) and then back to (44) ,we finally obtain

$$\frac{dz}{dt} = -\Gamma(s)(z - \tan(\beta\Omega(s)/2)), \tag{55}$$

where

$$\Gamma(s) = \Gamma_{0\to1} + \Gamma_{1\to0}, \quad \Gamma_{0\to1} = \Gamma_{1\to0} e^{-\beta\varepsilon(s)}. \tag{56}$$

Here $\Gamma_{1\to0}(s) = g_0(s)$ and

$$\Gamma_{1\to0}(s) = 2Re \int_0^\infty d\tau\, e^{i\Omega(s)\tau - \mathbb{h}(s) f(\tau,s)} F(\tau, s), \tag{57}$$

where the function f is given in (49) and (51) and the function F is given in (48) and (50). Equation (55) is a rate equation for the population difference with Γ_{10} (Γ_{01}) indicating the transition rate from the state 1 to 0 (0 to 1). This is a central result of our NIBA theory analysis.

Following [35], the criterion of applicability of NIBA is (cf. (54))

$$g_1 \ll 1. \tag{58}$$

In our case this amounts to the condition

$$g_1(s) = 2Re \int_0^\infty d\tau\, \tau\, e^{i\Omega(s)\tau - \mathbb{h}(s) f(\tau,s)} F(\tau, s) \ll 1. \tag{59}$$

We note that this condition corresponds to $\Gamma_{1\to0}\,\tau_b \ll 1$ because $\tau_b = 1/\mathbb{h}^{1/2}(s)W(s)$ is the size of the interval beyond which the integrand in (57) decays exponentially. As it was discussed in the previous section, we only need to inspect the condition (59) at the end of the thermalization region. For the sake of numeral investigation we define this by the value of $s \approx s_{eq}$ where the deviation of the system state from instantaneous Gibbs distribution is 1%. We then compute g_1 at various values of parameters with the results given in Fig. 13. It can be seen that $g_1 \ll 1$ in the entire parameter range under study. Figure 14 shows the probability of success versus $h_1 = [0.38, .., 0.6]$. Tunneling can only be present for $h_1 < 0.5$ when there is an energy barrier between the local and global minimum (seen as a bifurcation in the semi-classical energy landscape analysis, see Fig 6). We observe a good correspondence between the results of the NIBA Quantum Master Equation and the D-Wave data.

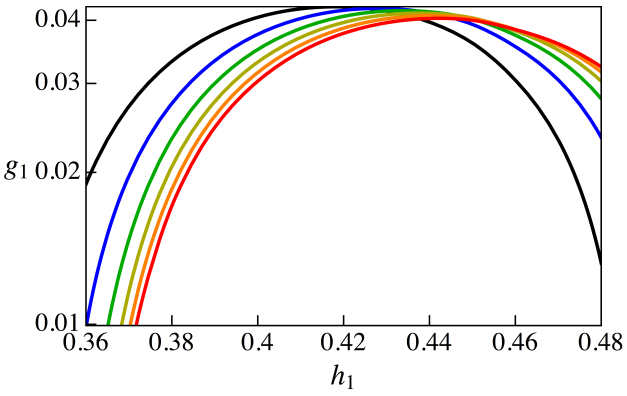

FIG. 13. Value of the coefficient g_1 in the NIBA criterion (58) as a function of the local field h_1/J at different temperatures. Black, blue, green, yellow, orange, and red curves correspond to the temperature values of 15.5, 20, 25, 30, 35, and 40 mK, respectively.

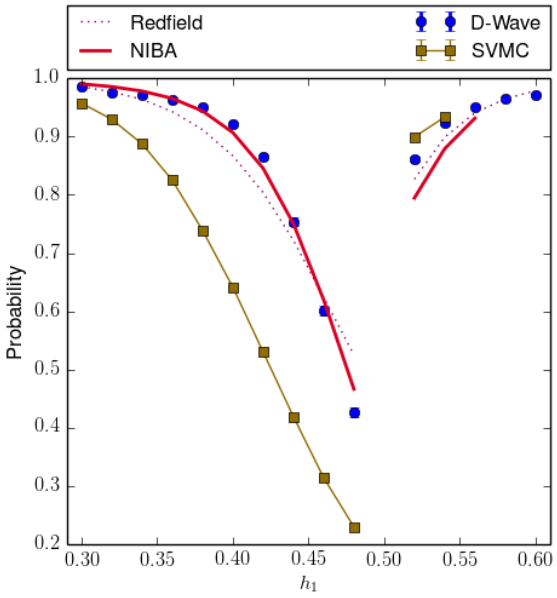

FIG. 14. Probability of success versus h_1 for D-Wave (purple ∘ marker), open system quantum numerics and the classical paths model (SVMC, brown □ marker). The open system numerics are Redfield (doted line) and the NIBA Quantum Master Equation (continuous red line). The NIBA Quantum Master Equation is a surprisingly good fit to the data. Error bars are smaller than markers.

C. Numerical simulation of classical paths

Our main purpose is to study multiqubit tunneling under experimental conditions with current technology for programmable quantum annealing, such as the D-Wave II chip. One important component of this study is the comparison to the detailed open quantum system theory outlined in the previous section. In addition, we will compare the experimental data with semiclassical numerics that simulate the evolution under the effective potential $U(q_1, q_2, s)$, as introduced in Sec. II B. We are interested in numerical methods that fulfill the following conditions:

- They must be constrained to quantum product states, entangled quantum states are disallowed.
- They do not include collective state or cluster updates. This prevents quantum tunneling to be included in the simulation. The dynamical equations of the numerical method must spec-

ify only equations of motion for each individual qubit in the product state

- The simulation must be capable of including the effective potential $U(q_1, q_2, s)$ of Sec. II B.

One such method was introduced recently in Ref. [41] and studied in related works [42, 43]. The dynamics are constrained to spin vector product states, with one spin per vector qubit. For a given product state, we denote by θ_j the angle of the spin vector for qubit j with the x quantization axis. For a given Hamiltonian $H_0(s)$, we denote the corresponding energy by $E_s(\theta_1, \ldots, \theta_N)$. The evolution consists in a sequence of sweeps along the Hamiltonian path $\{H_0(s)\}$. In each sweep, a Monte Carlo update is proposed for each qubit in the following manner:

- A new angle θ'_j is drawn from the uniform distribution in $[0, 2\pi]$.
- The spin vector for qubit j is updated $\theta_j \leftarrow \theta'_j$ according to the metropolis rule for the energy difference

$$D = E_s(\ldots, \theta'_j, \ldots) - E_s(\ldots, \theta_j, \ldots) \, .$$

That is, the move is always accepted if D is negative, and with probability given by the Boltzmann factor $\exp(-D/k_B T)$ if D is positive.

We call this method Spin Vector Monte Carlo (SVMC). The initial state is chosen to be the global minimum of the transverse field. When the spin vectors of each cluster are aligned with the parameters $\{q_1, q_2\}$ we obtain $E_s(q_1, \ldots, q_2) = U(q_1, q_2, s)$. For low T and sufficient sweeps, the evolution proceeds along the false minima path of Fig. 5. That is, the numerical method at low temperature simulates the classical paths model outlined in Sec. II B.

This numerical method allows us to study thermal hoping between the minima of the effective potential $U(q_1, q_2, s)$. To check this correspondence, we studied the height of the energy barrier obtained from Kramer's theory applied to SVMC. For the potential $U(q_1, q_2, s)$ at a fixed value of s, we initialized the spin vector state at a local minima, and watch for Kramer's events. A Kramer event corresponds to the arrival at the other minima under thermal activation. According to Kramer's theory, the dependence on temperature for the expected number of sweeps necessary for a Kramer's event follows the formula $\exp(\Delta U/T)$, where ΔU is the height of the energy barrier. We extract the energy barrier by fitting the curve of the average number of sweeps for different T. We find that this matches almost exactly the energy barrier height from $U(q_1, q_2, s)$ in Fig. 6 for different values of s, see Fig. 15. We also studied other semiclassical methods, such as a mean field Redfield model similar to Forster's theory, and a Landau-Lifshitz-Gilbert model related to the one studied in Ref. [44]. As we could not recover the barrier height of the effective energy potential $U(q_1, q_2, s)$ from the Kramer's events with this other numerical semiclassical methods, we will use SVMC in what follows.

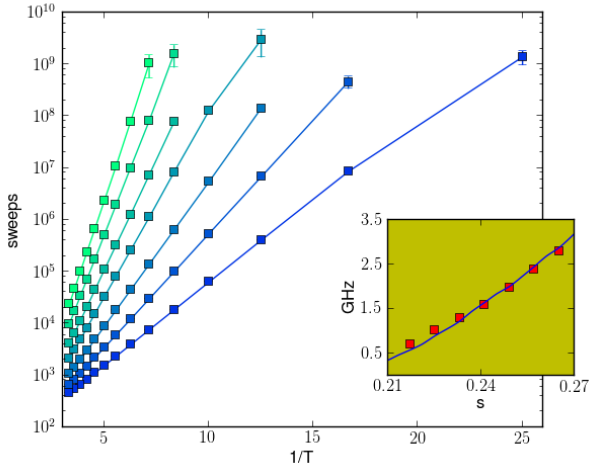

FIG. 15. Analysis of the Kramer's rate for SVMC. The main figure shows, in a semilog scale, the average number of sweeps as a function of temperature. We plot lines for different points in the annealing schedule, from $s = 0.217$ (dark blue) to $s = 0.265$ (green). The embedded figure shows the corresponding estimated energy barrier height from the Kramer's rate (red dots) and the semiclassical energy barrier (blue). There is a good correspondence between SVMC and the effective energy potential.

A disadvantage of SVMC as outlined above and introduced in Ref. [41] is that there is no natural choice to relate the number of sweeps to the physical evolution time. As in other works, we will choose the number of sweeps in order to obtain a good correlation with the probability of success of the D-Wave chip for a benchmark of random Ising models with binary couplings $J_{jk} \in \{1, -1\}$ [41, 43, 45, 46]. This will allow us to relate phenomenologically the number of sweeps to physical time. We set the algorithmic temperature of SVMC to be the same as the physical temperature because we are interested in the dependence of the success probability with temperature. There are no important differences for the correlation with other temperature choices. The correlation with the random Ising benchmark for 128K sweeps (see Fig. 16) is 0.92, and the residual probabilities $p_{\rm SVMC} - p_{\rm D-Wave}$ have a mean of 0.05 and a standard deviation of 0.12. This is on a par with the best values found over a wide range of parameters. We will use 128K sweeps at 15 mK as our reference rate for the rest of the paper.

Another parameter, the so-called qubit background susceptibility χ, has been introduced in the literature to improve the correlations between numerical simulations and the D-Wave data [42, 43]. While the physical motivation for this parameter is well understood, it is also treated in those works as a free parameter together with the number of sweeps. Increasing values of χ have the effect of decreasing the barrier height for $h_1 < J/2$. We have designed a specific problem to bound the range of choices of χ for SVMC compatible with experimental data. We find $\chi = 0.0025$ to be the value most consistent with the data for the device used in our paper, as seen App. D. Plots that include this choice of χ for SVMC are also presented in the

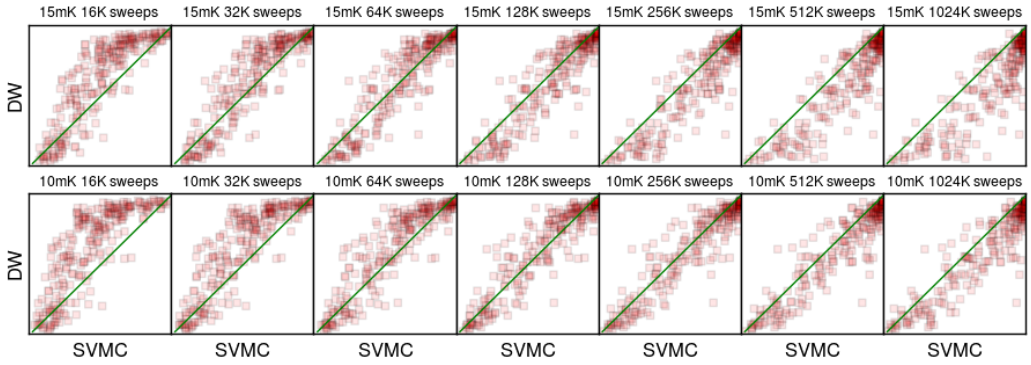

FIG. 16. Scatter plots showing the correlation of D-Wave II data for the random Ising benchmark for different algorithmic temperatures (in mK) and number of sweeps. We will use the parameters T = 15 mK, and sweeps = 128K in the rest of the paper.

Appendix.

IV. EXPERIMENTAL RESULTS FROM THE D-WAVE II PROCESSOR AND FIT TO THEORY

A. Double well potential with two clusters

One of the most distinctive signatures of quantum tunneling when compared to thermal hoping is the response to temperature variations at low temperatures. Consider first the quantum tunneling situation. For low temperatures compared to the gap and when the tunneling rate is fast compared to the evolution time, the final success probability is close to one. As we increase the temperature in the range of the gap, we expect to see thermal excitations and a lower probability of success. Therefore, the expected tendency at low temperatures is a decrease of probability of success with temperature. Consider now the situation with thermal hoping. At very low temperatures, the state follows the classical path along the local minimum through the evolution. If this path does not connect to the global minimun, the probability of success is close to zero. As we increase the temperature, we also increase the probability of a thermal excitation over the energy barrier, and therefore increase the probability of success. Consequently, the expected tendency at low temperatures is an increase in the probability of success for models that follow the classical paths.

Figure 17 shows the success probability as a function of temperature for D-Wave, open system quantum numerics and the classical paths model (SVMC) for $h_1 = 0.44$ in the Hamiltonian of Eq. (4). There is a clear tendency for lower probability of success at increasing temperature in the experimental D-Wave data. The same is true of the different open system quantum master equations. This is a consequence of quantum tunneling. Interestingly, SVMC shows a clear tendency for higher probability of success at increasing temperature. This is a consequence of thermal hoping above the energy barrier. The probability of success of SVMC is also lower than D-Wave data

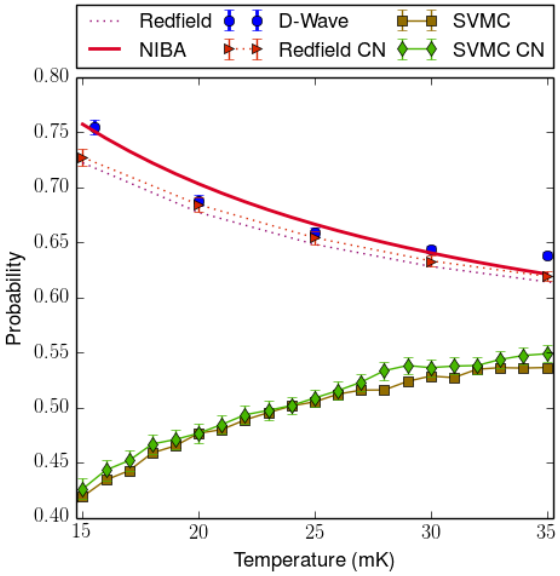

FIG. 17. Probability of success versus temperature at $h_1 = 0.44$ for D-Wave (purple ∘ marker), open system quantum numerics and the classical paths model (SVMC). The open system numerics are Redfield (doted line), Redfield with physically estimated control noise of $\sigma_h = 0.05$ for the local fields and $\sigma_J = 0.035$ for the couplings (doted line with ▷ marker) and the NIBA Quantum Master Equation (continuous red line). The two SVMC curves correspond to SVMC (brown □ marker) and SVMC with the physically estimated control noise of $\sigma_h = 0.05$ for the local fields and $\sigma_J = 0.035$ for the couplings (green ◊ marker). Error bars are smaller than markers when not seen.

at the same temperature. The probability of success obtained with the Redfield quantum master equation matches well the D-Wave data, and it is not affected by the control noise of the D-Wave chip. SVMC is ran at an algorithmic temperature equal to the physical temperature indicated in the horizontal axis, and with 128K sweeps, as explained in Sec. III C. We plot SVMC without control noise and SVMC with the physically estimated control noise. Averaging over control noise does not have a significant effect on the probability of success for SVMC. As seen in Fig-

ure 14, the NIBA Quantum Master Equation is a better match to the data than Redfield. In the region $h_1 < 0.5$ there is an energy barrier between the local and global minimum. In this region we see that the probability of success for SVMC is significantly lower than the probability of success for D-Wave and open system quantum models.

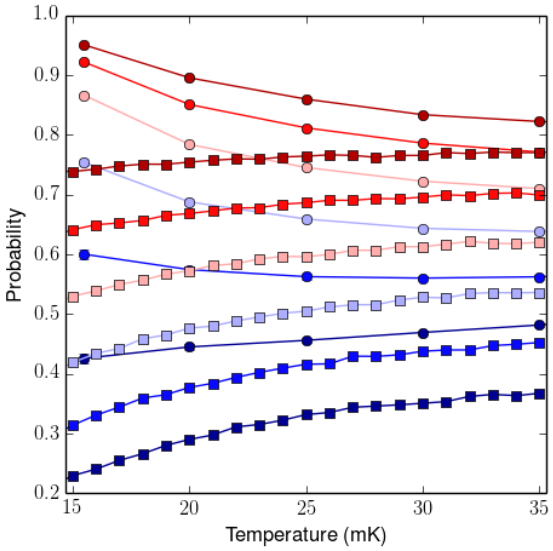

FIG. 18. Probability of success versus temperature for D-Wave data (∘ markers) and SVMC numerics (□ markers). We plot (from top to bottom, and red to blue) $h_1 = [0.38, 0.4, 0.42, 0.44, 0.46, 0.48]$. Error bars are smaller than markers. We use SVMC with 15 mK algorithmic temperature and 128K sweeps, as explained in the text.

Figure 18 shows the probability of success versus temperature for D-Wave data and SVMC numerics for $h_1 = [0.38, 0.4, 0.42, 0.44, 0.46, 0.48]$. The probability of success decreases with temperature for D-Wave in instances with a significant coherent tunneling contribution to the dynamics. For SVMC the probability of success increases with temperature in all cases. As noted before, the probability of success form SVMC is lower than the probability of success of D-Wave. Figure 19 shows the probability of success versus temperature for D-Wave data and open quantum systems numerics for the same values of h_1. The D-Wave data reproduces the decrease probability of succes predicted by the quantum models. The probability of success does increase with temperature for D-Wave for the instance with $h_1 = 0.48$, where the minimum gap is 10 MHz. The limitation in this case is strong coupling to low frequency noise. This behavior is not captured by standard Redfield theory. To explain it, we must take into account the reorganization energy induced by low frequency noise, as in standard Marcus theory. The NIBA Quantum Master Equation does capture this effect correctly. For this gap size coherent quantum tunneling is suppressed.

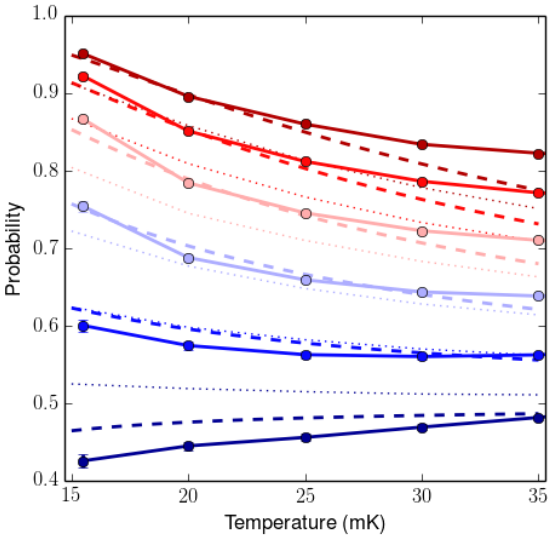

FIG. 19. Probability of success as a function of temperature for $h_1 = [0.38, 0.4, 0.42, 0.44, 0.46, 0.48]$. We plot D-Wave data (∘ markers), Redfield (dotted line) and the NIBA Quantum Master Equation (dashed line). The main qualitative difference is that for $h_1 = 0.48$ the NIBA Quantum Master Equation predicts a much lower probability of success, which increases with temperature. We see the same feature in D-Wave's experimental data. In the NIBA Quantum Master Equation, this is due to the suppression of the tunneling rate by the low-frequency noise. The gap at the avoided crossing for $h_1 = 0.48$ is 10 MHz. The standard Redfield model does not include low-frequency noise.

B. Larger problems that contain the weak-strong cluster "motives" as subproblems

In the previous sections we established that quantum tunneling assists the D-Wave II processor in finding the global minimum of the weak-strong cluster probe problem. The 16 qubit problem we considered was specifically designed to be suitable for studying the role of tunneling by analytical, numerical and experimental means. A generalization to a larger number of qubits is achieved by studying problems that contain the weak-strong cluster "motive" multiple times within the connectivity graph.

A first generalized configuration we studied is a stack of weak-strong cluster pairs with $h_1 = 0.4$ setting all connections between the left columns of the unit cells in the Chimera graph to ferromagnetic 1 (see Fig. 20a). As the number of stacked cluster pairs grows the success probability decreases for the annealing time of 20 μs that was used in the previous sections. This behavior is expected since the minimum gap also decreases. When we increase the anneal time to 20 ms the success probability grows significantly. The increase of the probability of success for SVMC is much slower with a proportional increase in the number of sweeps (note the logarithmic scale) even for instances with 128 qubits, see Fig. 21.

In a second experiment we again placed a number

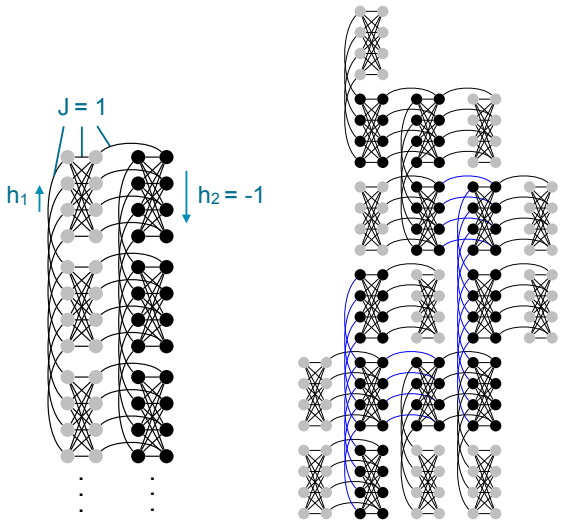

(a) Stacked clusters (b) Glass of weak-strong cluster pairs

FIG. 20. Larger problems that contain the weak-strong cluster "motives" as subproblems. (a) A stack of weak-strong cluster pairs. (b) Weak-strong cluster pairs connected in a glassy fashion by setting all connections between any two neighboring strong clusters randomly to either -1 or $+1$ The $+1$ connections are depicted in blue.

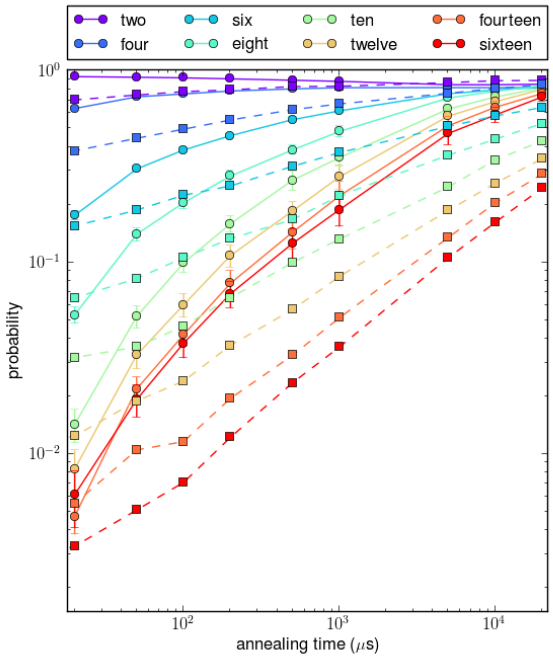

FIG. 21. Success probabilities for varying numbers of stacked weak-strong cluster pairs as a function of annealing time for a weak local field $h_1 = 0.4$. We show D-Wave data and SVMC. Note that for larger number of qubits the success probability for the D-Wave increases faster with annealing time than for SVMC with a proportional increase in the number of sweeps.

of weak-slow cluster pairs across the Chimera graph. Then we connected the strong clusters in a glass like structure by randomly setting all Chimera connections between neighboring pairs of strong clusters to $+1$ or -1. Fig. 20b depicts a problem instance constructed this way. The success probabilities are shown in Fig. 22. The fitting exponent for the D-Wave data is $-(1.1 \pm 0.05) \cdot 10^{-2}$, while the fitting exponent for the SVMC numerics is $-(2.8 \pm 0.17) \cdot 10^{-2}$. For additional data including problems for which the strong fields have been set to zero please refer to Appendix C.

V. CONCLUSION

It has been a subject of heated debate whether quantum resources in the D-Wave II processor are employed in a manner that increases the probability of the quantum annealing process to return low energy solutions of the encoded optimization problem. To make progress answering this question we studied the simplest non-convex optimization problem that only exhibits one false and one global minimum in a time dependent effective potential. The time evolution is such that a path in the potentical over product states connects the initial global minimum with the final false minimum. The final global minimum can only be reached by traversing an energy barrier. Experimentally we found that for this situation the D-Wave II quantum annealer returns the solution that minimizes the energy with higher probability than physically plausible models of the hardware that only employ product states which do not allow for multiqubit tunneling transitions. On the contrary open system quantum mechanical models fit the hardware data well. We developed a NIBA Quantum Master Equation which takes high and low frequency noise into account. It continuously rotates the basis it employs to coincide with the basis that minimizes the transition rate between the first two levels. In this way we find the most robust states under decoherence. One can think of this as working in the instantaneous pointer basis [37, 47]. The polaron transform was used since the interaction of the qubits with their oscillator baths forms polaron-like quasi particles. To increase our confidence that quantum mechanical models are indeed required to describe the annealing dynamics properly we added a series of experiments in which we varied the temperature of the chip. Independent of specific choices in the quantum models or the classical models the prediction is that the probabilities to find the system in the lowest energy state should decrease with increasing temperature for a quantum system but should increase for a classical paths model. This is indeed observed.

The correlation between D-Wave's experimental data and Quantum Annealing Quantum Monte Carlo (QAQMC) has been studied in recent works [43, 45, 46]. Unfortunately, we do not have at the present time a detailed theoretical connection between the Monte Carlo updates in QAQMC and the open system quantum dynamics. The relation between QAQMC and quantum tunneling is also not well understood. We show in Fig. 23 the probabilities for QAQMC as a

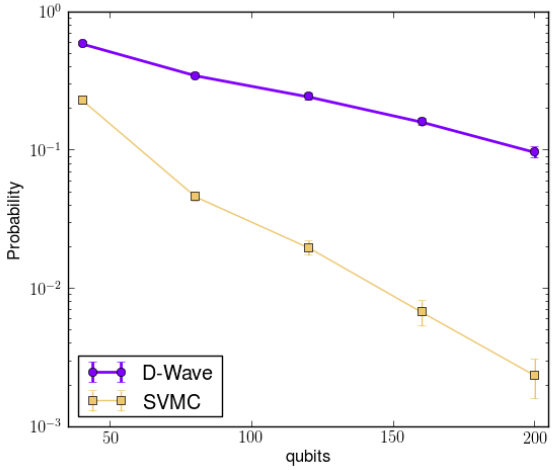

FIG. 22. Success for a glass of weak-strong clusters as a function of the number of qubits involved. D-Wave data is plotted with purple ∘ markers. SVMC is plotted with □ markers. The fitting exponent for the D-Wave data is $-(1.1 \pm 0.05) \cdot 10^{-2}$, while the fitting exponent for the SVMC numerics is $-(2.8 \pm 0.17) \cdot 10^{-2}$. The error estimates for the exponents are obtained by bootstrapping.

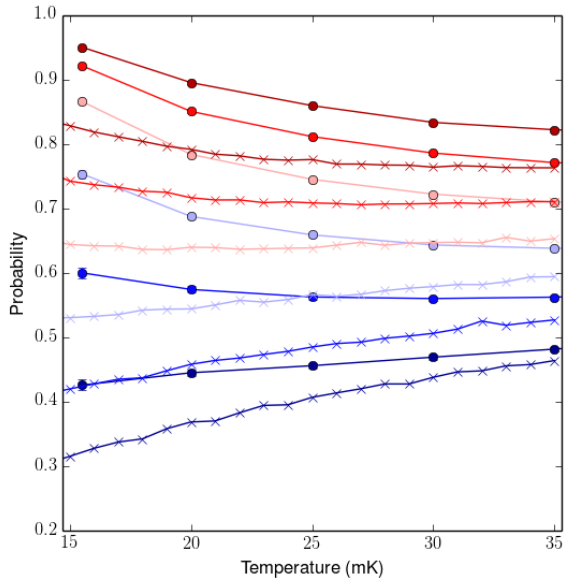

FIG. 23. Probability of success versus temperature for D-Wave data (∘ markers) and Quantum Annealing Quantum Monte Carlo (QAQMC) numerics (× markers). We plot (from top to bottom, and red to blue) $h_1 = [0.38, 0.4, 0.42, 0.44, 0.46, 0.48]$. Error bars are smaller than markers. QAQMC is not a good fit to D-Wave's data.

function of temperature for different values of h_1. We use the similar parameters for QAQMC as in Ref. [45]. The probability of success for QAQMC is lower then for D-Wave. On the one hand, the temperature dependence of the probability of success is decreasing for small h_1/J ratios (big minimum gaps in the QA spectrum). On the other hand, this dependence is opposite to D-Wave's data for $h_1 = 0.44$, the main case studied in Sec. IV A.

Beyond the original 16 qubit probe problem we also explore larger problems that contain multiple weak-strong cluster pairs. We found that classical paths models that only operate on product states do not explain the hardware performance.

A way to think of multiqubit cotunneling as a computational resource is to regard it as a form of large neighborhood search. Cotunneling transitions involving K qubits explore a K variable neighborhood. We found that the current generation D-Wave II annealer enables tunneling transitions involving at least 8 qubits. It will be an important future task to determine the maximal K for the current hardware and how large it can be made in next generation hardware. The larger K the easier it should be to translate the quantum resource "K-qubit cotunneling" into a computational speedup. We want to emphasize that we do not claim to have established a quantum speedup in this work. To this end one would have to demonstrate that no known classical algorithm finds the optimal solution as fast as the quantum process. To establish such an advantage it will be important to study to what degree cotunneling can be emulated in classical algorithms by employing cluster update methods. However the cotunneling phenomena demonstrated here present a big step towards what we would like to call a *physical speedup*: a speedup relative to a hypothetical version of the hardware operated under the laws of classical physics.

Acknowledgements – We would like to thank Ryan Babbush, Edward Farhi and John Martinis for reviewing and discussing earlier versions of the paper. The work of V.N.S. was supported in part by the Office of the Director of National Intelligence (ODNI), Intelligence Advanced Research Projects Activity (IARPA), via IAA 145483 and by the AFRL Information Directorate under grant F4HBKC4162G001.

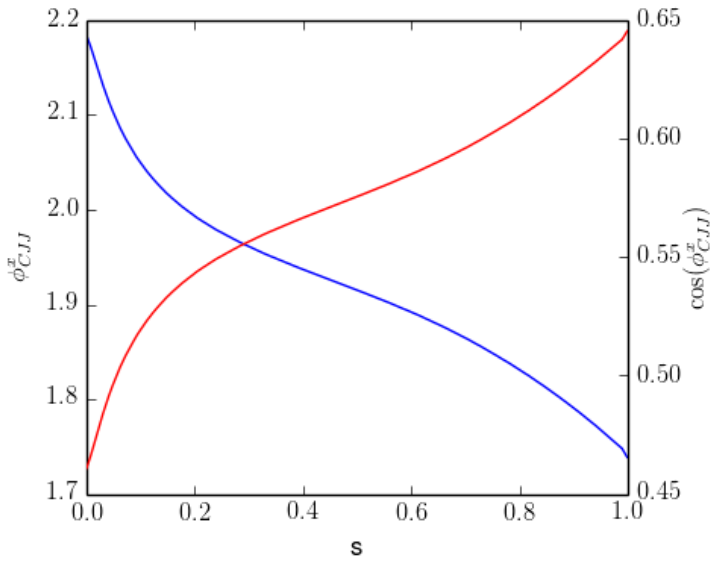

FIG. 24. The CJJ external phase ϕ^x_{CJJ} and $\cos(\phi^x_{\mathrm{CJJ}})$.

Appendix A: Single Flux Qubit Hamiltonian

1. Full Flux Qubit Hamiltonian

The full Compound Josephson Junction flux qubit Hamiltonian is better expressed in terms of flux phases, defined as renormalized fluxes $\phi = 2\pi\Phi/\Phi_0$ for any flux Φ. The Hamiltonian is [10]

$$-E_{\mathrm{C}}\partial^2_{\phi} - E_{\mathrm{C_{CJJ}}}\partial^2_{\phi_{\mathrm{CJJ}}} + E_{\mathrm{J}}\cos(\phi)\cos(\phi_{\mathrm{CJJ}}/2) + E_{\mathrm{L}}\frac{(\phi-\phi^x)^2}{2} + E_{\mathrm{L_{CJJ}}}\frac{(\phi_{\mathrm{CJJ}}-\phi^x_{\mathrm{CJJ}})^2}{2}\,, \tag{A1}$$

where ϕ is the body flux phase to be quantized, ϕ^x is the external flux phase, ϕ_{CJJ} is the flux phase of the Compound Josephson Junction and ϕ^x_{CJJ} is the external flux of the Compound Josephson Junction (CJJ). The energies of the different terms are given by

$$E_{\mathrm{C}} = \tfrac{(2e)^2}{2C} \qquad E_{\mathrm{C_{CJJ}}} = \tfrac{(2e)^2}{2(C/2)} \qquad E_{\mathrm{J}} = \tfrac{I_c\Phi_0}{2\pi} \qquad E_{\mathrm{L}} = \left(\tfrac{\Phi_0}{2\pi}\right)^2 \tfrac{1}{L+L_{\mathrm{CJJ}}/4} \qquad E_{\mathrm{L_{CJJ}}} = \left(\tfrac{\Phi_0}{2\pi}\right)^2 \tfrac{1}{L_{\mathrm{CJJ}}}\,.$$

The parameters are the capacitance of the Compound Josephson Junction C, the body inductance of the main flux loop L and of the Compound Josephson Josephson L_{CJJ}, and the effective critical current of the Compound Josephson Junction I_c.

The median values for D-Wave's Compound Josephson Junction flux qubits in GHz are

$$\tfrac{E_{\mathrm{C}}}{2\pi\hbar} = 0.67 \text{ GHz} \qquad \tfrac{E_{\mathrm{C_{CJJ}}}}{2\pi\hbar} = 1.35 \text{ GHz} \qquad \tfrac{E_{\mathrm{J}}}{2\pi\hbar} = 1071 \text{ GHz} \qquad \tfrac{E_{\mathrm{L}}}{2\pi\hbar} = 537 \text{ GHz} \qquad \tfrac{E_{\mathrm{L_{CJJ}}}}{2\pi\hbar} = 11680 \text{ GHz}\,.$$

The CJJ flux phase ϕ^x_{CJJ} controls the quantum annealing evolution. Its value $\phi^x_{\mathrm{CJJ}}(s)$ as a function of the annealing parameter for the quantum annealing schedule employed in this paper is plotted in Fig. 24.

Because $E_{\mathrm{L_{CJJ}}} \gg E_{\mathrm{L}}$ the phase ϕ_{CJJ} can be assumed to be centered at the value given by ϕ^x_{CJJ}, to a first approximation. The approximated flux qubit Hamiltonian is then

$$\mathcal{H}_s(\phi^x) = -E_{\mathrm{C}}\partial^2_{\phi} + E_{\mathrm{J}}\cos(\phi)\cos(\phi^x_{\mathrm{CJJ}}(s)/2) + E_{\mathrm{L}}\frac{(\phi-\phi^x)^2}{2}\,. \tag{A2}$$

This potential is plotted in Fig. 25a.

2. Effective qubit Hamiltonian

The effective qubit Hamiltonian is the simplified Hamiltonian $\mathcal{H}_s(\phi^x)$ of Eq. (A2) projected into the two lowest energy energy levels $\{|\mathfrak{g}(s)\rangle, |\mathfrak{e}(s)\rangle\}$ of $\mathcal{H}_s(0)$

$$\mathcal{H}_s(\phi_x)\Big|_{\{|\mathfrak{g}(s)\rangle,|\mathfrak{e}(s)\rangle\}} = \mathcal{H}_s(0) + \phi^x\frac{\partial\mathcal{H}_s(0)}{\partial\phi^x}\Big|_{\{|\mathfrak{g}(s)\rangle,|\mathfrak{e}(s)\rangle\}}\,. \tag{A3}$$

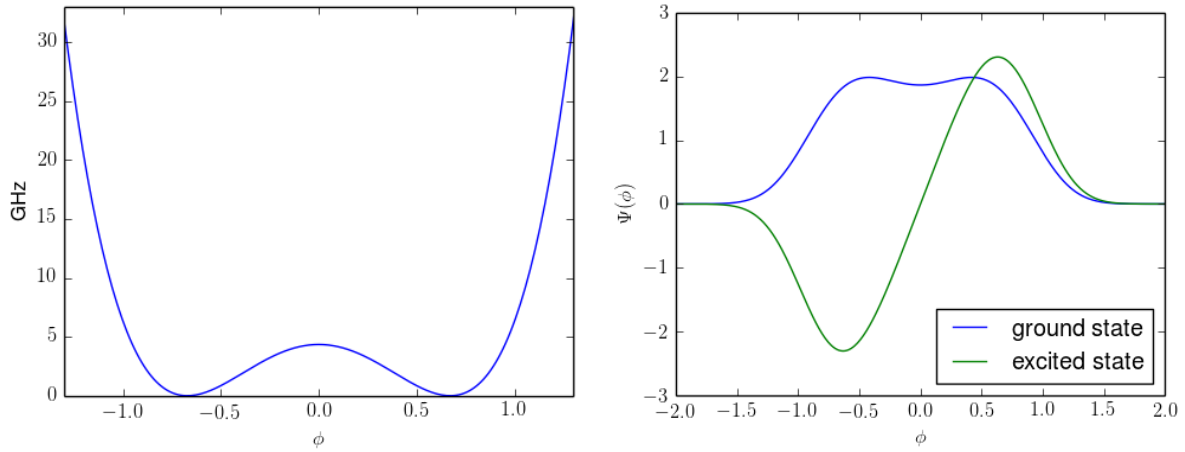

(a) Simplified 1D potential.

(b) First two eigenstates.

FIG. 25. (a) The simplified 1D potential $\mathcal{H}(\phi^x)$ of Eq. (A2) for annealing parameter $s = 0.278$. (b) The first two eigenvectors of the flux qubit potential for $s = 0.278$.

The eigenvectors of $\mathcal{H}_s(0)$ are symmetric and anti-symmetric superpositions of the flux up and down state in the double well potential (see Fig. 25b)

$$|\mathfrak{g}(s)\rangle = \frac{1}{2}(|\uparrow(s)\rangle + |\downarrow(s)\rangle) \tag{A4}$$

$$|\mathfrak{e}(s)\rangle = \frac{1}{2}(|\uparrow(s)\rangle - |\downarrow(s)\rangle)\ . \tag{A5}$$

The gap between the ground state and the third excited state, depending on the annealing parameter s, goes between 10 and 8 GHz in the region of interest. This justifies the projection into the two lowest energy levels as long as the linear term in ϕ_x remains well below this energy.

Note that

$$\phi^x \frac{\partial \mathcal{H}_s(0)}{\partial \phi^x} = \Phi^x \frac{\Phi}{L + L_{\rm CJJ}/4}\ , \tag{A6}$$

where Φ^x is the external flux and $\Phi/(L + L_{\rm CJJ}/4)$ is the persistent current operator. The eigenvectors of this operator are the flux up and down states $|\uparrow(s)\rangle, |\downarrow(s)\rangle$, with eigenvalues $\pm I_p(s)$. This defines the persistent current $I_p(s)$. We denote the gap between these states by Δ_s. In the basis of the up and down flux states we write

$$\mathcal{H}_s(0) + \phi^x \frac{\partial \mathcal{H}_s(0)}{\partial \phi^x}\Big|_{\{|\mathfrak{g}(s)\rangle, |\mathfrak{e}(s)\rangle\}} = -\frac{1}{2}(\Delta_s \sigma^x + \epsilon_s(\phi^x)\sigma^z)\ , \tag{A7}$$

with $\epsilon_s(\phi^x) = 2I_p(s)\Phi^x$.

3. External flux phase ϕ^x

The value of the external flux phase ϕ^x controls the strength of the local field in the single qubit Hamiltonian of Eq. (A7). In order to keep the local field synchronized with the coupling energy as explained in Ref. [11] (see also below), this value is chosen as

$$\phi^x(s) = (-h) M_{\rm AFM} I_p(s) \frac{2\pi}{\Phi_0}\ , \tag{A8}$$

where $h \in [-1, 1]$ is the dimensionless value of the local field (with the sign convention $H \sim h\sigma^z$), $M_{\rm AFM}$ is the experimental maximum anti-ferromagnetic coupling, and $I_p(s)$ is the expected value of the persistent current operator defined above. In our case $M_{\rm AFM} = 1.41$ pico henries. For the current schedule in the Google-NASA chip we have

$$M_{\rm AFM} I_p(s) \frac{2\pi}{\Phi_0} \approx 10^{-3}(4.11s + 1.21)\ . \tag{A9}$$

4. Coupling between qubits

The coupling between qubits has the form [48]

$$J_{ij}E_{\rm M}(\phi_i-\phi_i^x)(\phi_j-\phi_j^x)\approx J_{ij}E_{\rm M}\phi_i\phi_j\ , \tag{A10}$$

where $J_{ij}\in[-1,1]$ is the dimensionless coupling. The corresponding energy is

$$\frac{E_{\rm M}}{2\pi\hbar}=\frac{1}{2\pi\hbar}\left(\frac{\Phi_0}{2\pi}\right)^2\frac{M_{\rm AFM}}{(L+L_{\rm CJJ}/4)^2}=2.44\ {\rm GHz}\ . \tag{A11}$$

In the two level qubit Hamiltonian approximation we use the persistent current operator (the expectation of the flux divided by the inductance) to write

$$J_{ij}E_{\rm M}\phi_i\phi_j\approx J_{ij}M_{\rm AFM}I_p(s)^2\sigma_i^z\sigma_j^z=B(s)J_{ij}\sigma_i^z\sigma_j^z\ , \tag{A12}$$

with the annealing function defined as $B(s)=M_{\rm AFM}I_p(s)^2$. Note that this scales with the persistent current square. This is the reason why the external field flux is chosen (using our sign convention) as $\Phi^x=(-h)M_{\rm AFM}I_p(s)$ so then

$$\epsilon_s(\phi^x)=2(-h)M_{\rm AFM}I_p(s)^2=2(-h)B(s)\ . \tag{A13}$$

5. Coupling to the bath

The interaction Hamiltonian with the bath is dominated by fluctuations on the flux body bias. The dimensional interaction Hamiltonian is

$$\mathcal{H}_{\rm SB}=\hat{I}\delta\Phi_x=\frac{\hat{\Phi}-\Phi_x}{L}\delta\Phi_x\ . \tag{A14}$$

Projecting into the subspace $\{|\mathfrak{g}(s)\rangle,|\mathfrak{e}(s)\rangle\}$ as before we write

$$\mathcal{H}_{\rm SB}(s)=I_p(s)\sigma^z\delta\Phi_x=\frac{1}{2}\sigma^zQ(s) \tag{A15}$$

where

$$Q(s)=2I_p(s)\delta\Phi_x\ . \tag{A16}$$

The flux bias fluctuations is measured using microscopic resonant tunneling (MRT) techniques as explained in Sec. III A. In particular MRT is performed at a point s with small tunneling amplitude $\Delta<1$ MHz. Under these conditions we obtain the parameters for the noise spectral density $S^{\rm MRT}(\omega)$ which is defined in Eq. (15) as the correlation of $Q({\rm MRT})$. From Eq. A16

$$\delta\Phi_x=\frac{Q({\rm MRT})}{2I_p({\rm MRT})}\ , \tag{A17}$$

which implies

$$Q(s)=\frac{I_p(s)}{I_p({\rm MRT})}Q({\rm MRT})\approx\frac{I_p(s)}{I_p(1)}Q({\rm MRT})\ . \tag{A18}$$

This is the source of the dependence of the noise parameters in the annealing parameter, as mentioned in the text.

Appendix B: Villain representation

In the spin basis $|M,S\rangle$ for total spin S, we introduce scaled spin operators ${\rm s}^\alpha=S^\alpha/S$ for $\alpha=x,y,z$, and $q=M/S$ an scaled quantum number. Denote $\epsilon=1/S$ and

$${\rm s}^z|q\rangle=q|q\rangle \tag{B1}$$

$${\rm s}^\pm|q\rangle=\sqrt{q+\epsilon-q(q\pm\epsilon)}|q\pm\epsilon\rangle\ . \tag{B2}$$

We further introduce the canonically conjugated momentum operator $p = -i\,\epsilon\,\frac{\partial}{\partial q}$. The Villain representation in the limit of small ϵ (big n) is [49, 50]

$$\mathrm{s}^+ = e^{-ip}\sqrt{1+\epsilon-q(q+\epsilon)} \tag{B3}$$

$$\mathrm{s}^- = \sqrt{1+\epsilon-q(q+\epsilon)}e^{ip}\ . \tag{B4}$$

These operators are Hermitian conjugates in this representation, and we will see that they have the correct action in coordinate representations of the wave form

$$|\Psi\rangle = \int dq\ \Psi(q)|q\rangle\ . \tag{B5}$$

We will use the property

$$e^{-\epsilon\frac{\partial}{\partial q}}F(q) = \sum_{a=0}^{\infty}\frac{(-\epsilon)^n}{n!}\frac{\partial^n}{\partial q^n}F(q) = F(q-\epsilon)\ . \tag{B6}$$

We get

$$\mathrm{s}^+|\Psi\rangle = \int dq\ e^{-\epsilon\frac{\partial}{\partial q}}\sqrt{1+\epsilon-q(q+\epsilon)}\ \Psi(q)|q\rangle = \int dq\ \sqrt{1+\epsilon-(q-\epsilon)q}\ \Psi(q-\epsilon)|q\rangle \tag{B7}$$

$$= \int dq\ \sqrt{1+\epsilon-q(q+\epsilon)}\ \Psi(q)|q+\epsilon\rangle\ , \tag{B8}$$

and also

$$\mathrm{s}^-|\Psi\rangle = \int dq\ \sqrt{1+\epsilon-q(q+\epsilon)}e^{\epsilon\frac{\partial}{\partial q}}\ \Psi(q)|q\rangle\ = \int dq\ \sqrt{1+\epsilon-q(q+\epsilon)}\ \Psi(q+\epsilon)|q\rangle \tag{B9}$$

$$= \int dq\ \sqrt{1+\epsilon-q(q-\epsilon)}\ \Psi(q)|q-\epsilon\rangle \tag{B10}$$

Ignoring factors of order ϵ in Eqs. (B3) and (B4) we approximate

$$\mathrm{s}^x = \frac{1}{2}(\mathrm{s}^+ + \mathrm{s}^-) \approx \sqrt{1-q^2}\cos p\ . \tag{B11}$$

We can check the adequacy of the semi-classical Hamiltonian even for small numbers of spins from the qualitative agreement of the gap of the original Hamiltonian and that obtained from the semiclassical Hamiltonian by the standard instanton method [5, 49, 50]. From the definition of the momentum operator $p = -i\,\epsilon\,\frac{\partial}{\partial q}$ we see that $\epsilon = 1/S$ plays the role of $\hbar$ in the WKB approximation, and we write the WKB ansatz for the semiclassical eigenstates $\Psi \propto \exp(W/\epsilon)$. The semiclassical Hamiltonian is

$$-m(q,t)(\cos p - 1) + V(q,t)\ , \tag{B12}$$

where the effective q dependent mass is

$$m(q,t) = A(t)\sqrt{1-q^2}/\epsilon\ . \tag{B13}$$

Using the instanton technique, the gap can be estimated as

$$R\exp\left(-\frac{1}{\epsilon}\int_{q_a}^{q_b} dq\,p(q)\right)\ , \tag{B14}$$

where the exponent is the Euclidean action and $p(q)$ is the instanton trajectory between the double well minima q_a and q_b. The instanton trajectory is obtained by going to imaginary time, which gives the mapping $p \to -ip$. The instanton trajectory is obtained by solving

$$m(q,t)\,(1-\cosh p) + V(q,t) = V(q_a,t)\ . \tag{B15}$$

We obtain

$$p(q) = \cosh^{-1}\left(\frac{V(q,t)-V(q_a,t)}{m(q,t)}+1\right)\ . \tag{B16}$$

For the WKB attempt rate R we use the separation between the first and third eigenstates of the quantum Hamiltonian, $R \approx 3$ GHz, as a proxy for the gap of the possible single well bound states. Plugging into Eq. (B14), we obtain a sufficient qualitative agreement with the exact gaps

h_1	exact gap	instanton gap
0.48	10 MHz	5 MHz
0.47	36 MHz	33 MHz
0.46	78 MHz	85 MHz

(B17)

The agreement improves for increasing n [5, 49, 50]

Appendix C: Further comparisons of larger problems that contain the weak-strong cluster "motives" as subproblems.

1. SVMC and PIMC-QA results compared against D-Wave results

Figs. 26-31 show comparisons of SVMC (with and without χ-correction) and PIMC-QA against D-Wave results on the larger problems that contain the weak-strong cluster "motives" as subproblems. At each problem size (40, 80, 120, 160, and 200 spins) we tested 100 random instances. D-Wave was executed with 16 gauges at each instance. SVMC and PIMC-QA were each executed with 9 different parameters settings: 3 values for *steps* and 3 values for β. The plotted results were obtained by bootstrapping over the success probabilities obtained from individual instances and the error bars represent the bootstrapped estimate of standard error. The standard Student's T-test ($\alpha = 0.05$) was applied to verify the statistical significance of the difference in means between SVMC/PIMC-QA and D-Wave results. The null hypothesis was rejected at all parameter settings except for SVMC with χ-correction and $steps = 512$, $beta = 2.4$, $size = 5$ on the problem without strong fields.

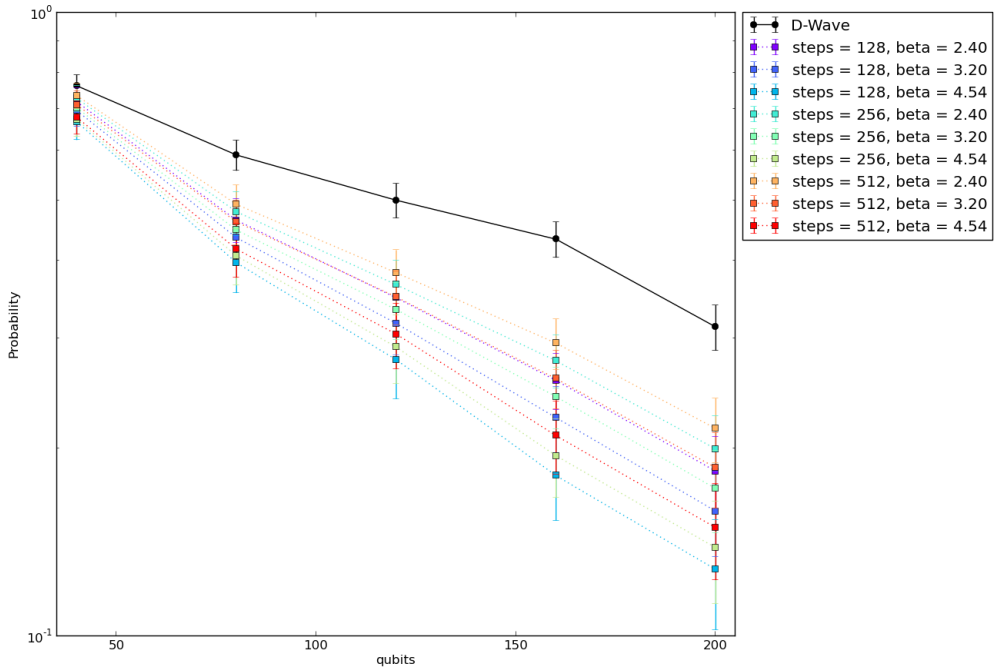

FIG. 26. D-Wave and SVMC (without χ-correction) results for instances without strong fields.

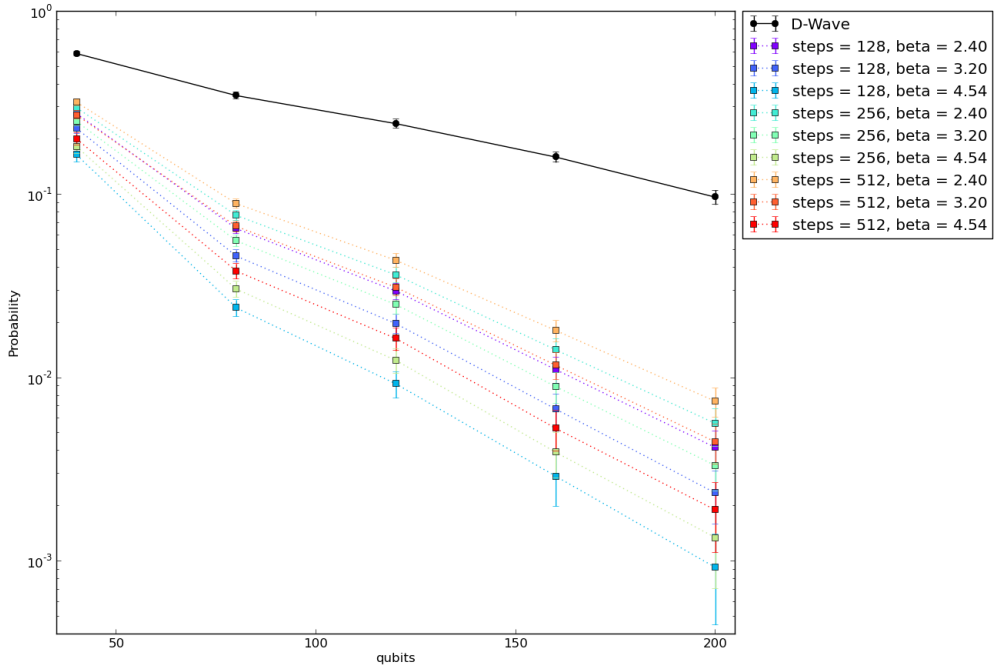

FIG. 27. D-Wave and SVMC (without χ-correction) results for instances with strong fields.

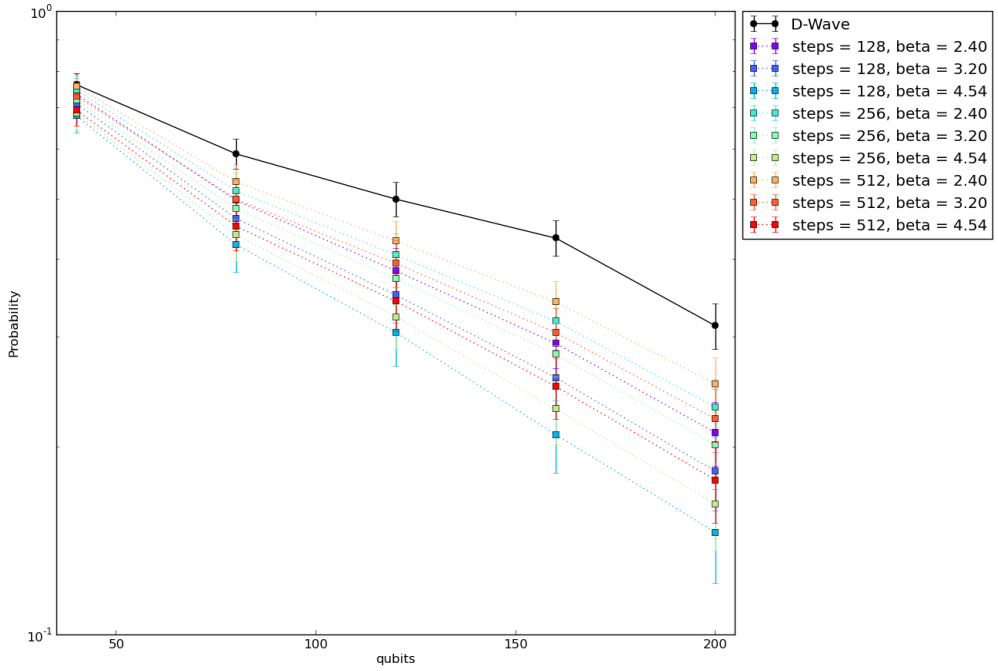

FIG. 28. D-Wave and SVMC (with χ-correction) results for instances without strong fields.

2. Fitting curves

In order to obtain a rough estimate of scaling behavior, we performed bootstrapped linear fits on the logs of success probabilities obtained from the same instances whose results are shown in Figs. 26-31.

The resulting exponential fits in linear probability space for D-Wave are:

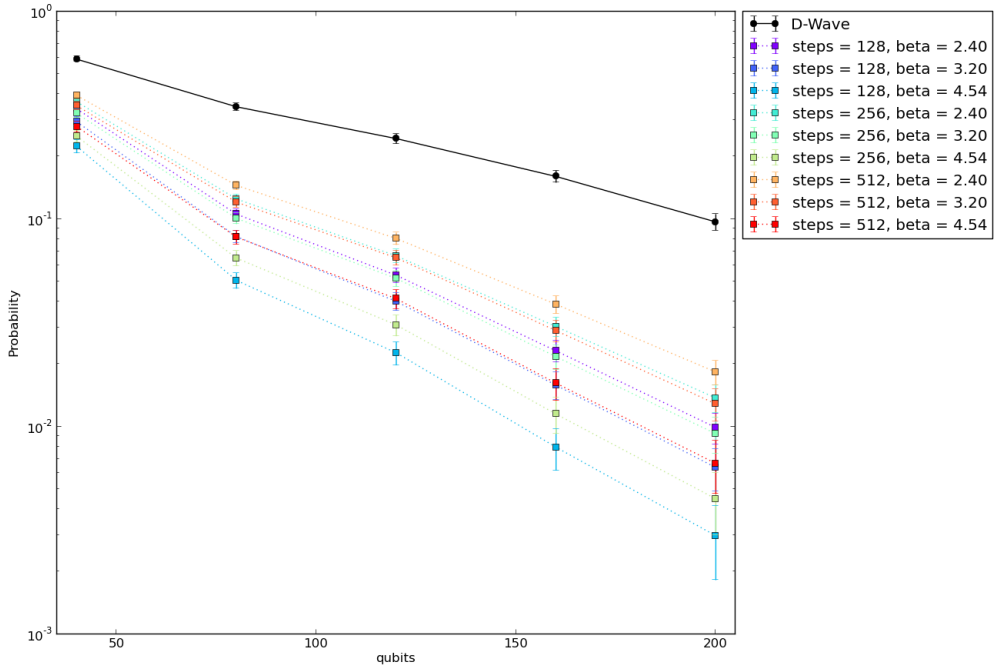

FIG. 29. D-Wave and SVMC (with χ-correction) results for instances with strong fields.

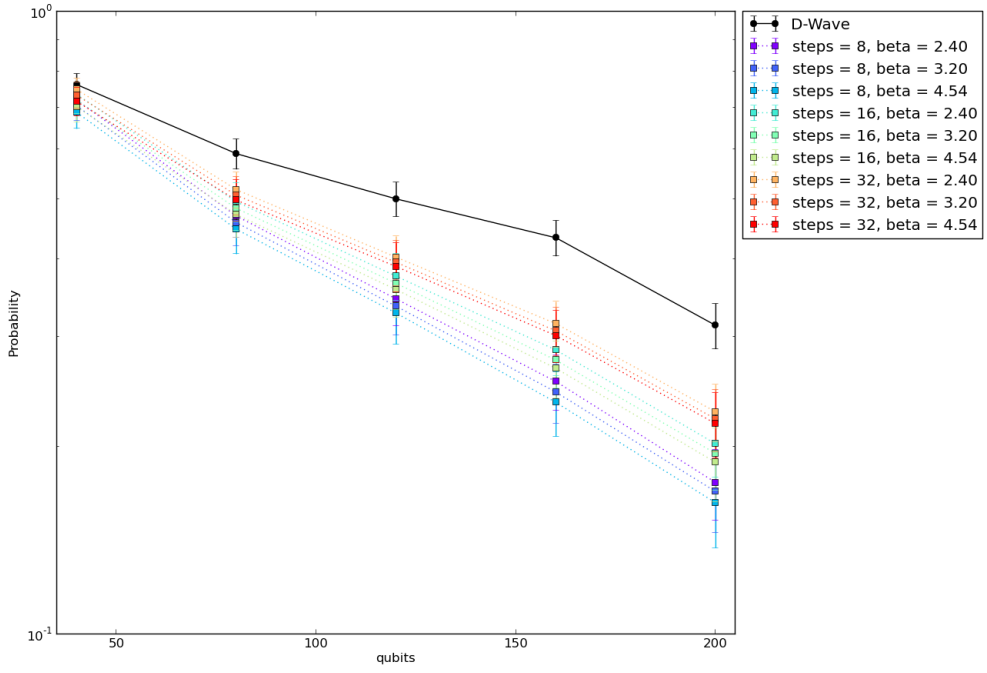

FIG. 30. D-Wave and PIMC-QA results for instances without strong fields.

- Without strong fields: $y(x) = e^{-0.0710 \pm 0.0573} e^{(-0.0052 \pm 0.0005)x}$
- With strong fields: $y(x) = e^{-0.1174 \pm 0.0498} e^{(-0.0110 \pm 0.0005)x}$

Additionally, Tables I-VI show the corresponding fitting coefficients (in log probability space) done also on the SVMC and PIMC-QA results.

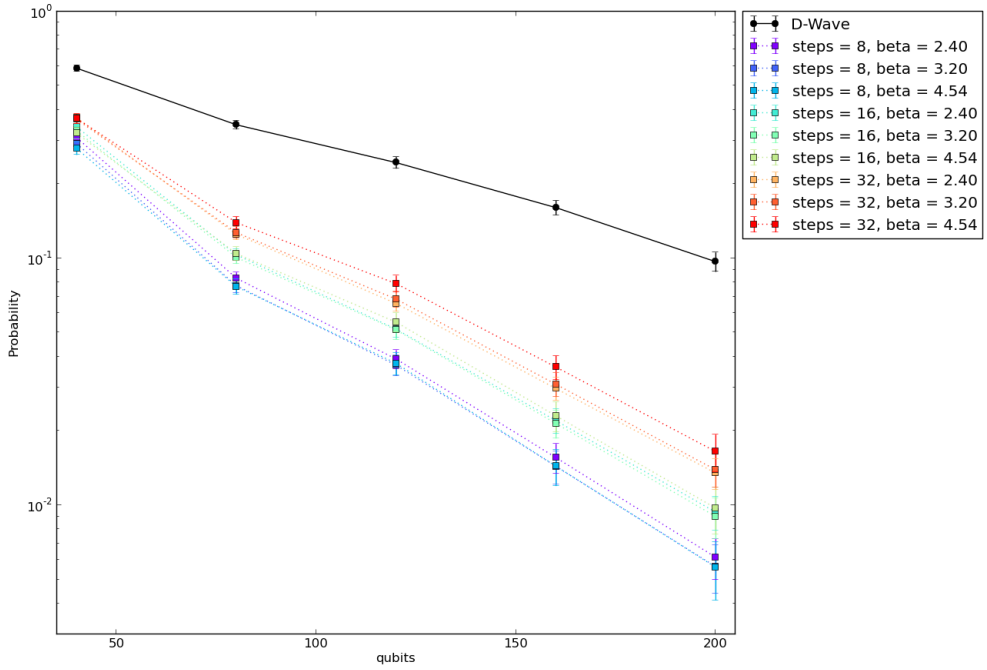

FIG. 31. D-Wave and PIMC-QA results for instances with strong fields.

steps\β	2.4	3.2	4.54
128	$(-0.0083 \pm 0.0008) * x - 0.0430 \pm 0.0823$	$(-0.0091 \pm 0.0009) * x - 0.0480 \pm 0.0948$	$(-0.0103 \pm 0.0012) * x - 0.0440 \pm 0.1146$
256	$(-0.0079 \pm 0.0008) * x - 0.0491 \pm 0.0783$	$(-0.0086 \pm 0.0009) * x - 0.0561 \pm 0.0903$	$(-0.0098 \pm 0.0011) * x - 0.0552 \pm 0.1102$
512	$(-0.0075 \pm 0.0007) * x - 0.0533 \pm 0.0744$	$(-0.0082 \pm 0.0008) * x - 0.0617 \pm 0.0856$	$(-0.0094 \pm 0.0010) * x - 0.0633 \pm 0.1050$

TABLE I. SVMC without χ-correction and without strong fields

steps\β	2.4	3.2	4.54
128	$(-0.0255 \pm 0.0012) * x - 0.4461 \pm 0.1065$	$(-0.0280 \pm 0.0017) * x - 0.5607 \pm 0.1471$	$(-0.0320 \pm 0.0029) * x - 0.8125 \pm 0.2404$
256	$(-0.0242 \pm 0.0011) * x - 0.4118 \pm 0.0961$	$(-0.0265 \pm 0.0015) * x - 0.5150 \pm 0.1300$	$(-0.0304 \pm 0.0026) * x - 0.7377 \pm 0.2167$
512	$(-0.0229 \pm 0.0010) * x - 0.3810 \pm 0.0880$	$(-0.0251 \pm 0.0013) * x - 0.4689 \pm 0.1157$	$(-0.0287 \pm 0.0023) * x - 0.6755 \pm 0.1907$

TABLE II. SVMC without χ-correction and with strong fields

steps\β	2.4	3.2	4.54
128	$(-0.0076 \pm 0.0007) * x - 0.0402 \pm 0.0729$	$(-0.0083 \pm 0.0008) * x - 0.0495 \pm 0.0843$	$(-0.0095 \pm 0.0010) * x - 0.0519 \pm 0.1026$
256	$(-0.0071 \pm 0.0006) * x - 0.0451 \pm 0.0682$	$(-0.0077 \pm 0.0008) * x - 0.0567 \pm 0.0790$	$(-0.0089 \pm 0.0009) * x - 0.0640 \pm 0.0972$
512	$(-0.0066 \pm 0.0006) * x - 0.0483 \pm 0.0639$	$(-0.0072 \pm 0.0007) * x - 0.0618 \pm 0.0742$	$(-0.0083 \pm 0.0009) * x - 0.0726 \pm 0.0916$

TABLE III. SVMC with χ-correction and without strong fields

steps\β	2.4	3.2	4.54
128	$(-0.0215 \pm 0.0009) * x - 0.3469 \pm 0.0830$	$(-0.0234 \pm 0.0013) * x - 0.4257 \pm 0.1095$	$(-0.0267 \pm 0.0021) * x - 0.6079 \pm 0.1764$
256	$(-0.0200 \pm 0.0008) * x - 0.3166 \pm 0.0744$	$(-0.0217 \pm 0.0011) * x - 0.3830 \pm 0.0962$	$(-0.0248 \pm 0.0018) * x - 0.5419 \pm 0.1535$
512	$(-0.0187 \pm 0.0007) * x - 0.2868 \pm 0.0672$	$(-0.0202 \pm 0.0010) * x - 0.3438 \pm 0.0857$	$(-0.0229 \pm 0.0015) * x - 0.4808 \pm 0.1327$

TABLE IV. SVMC with χ-correction and with strong fields

Based on these fits, the ratios between scalings of SVMC/PIMC-QA and corresponding scalings of D-Wave were computed and are summarized as follows:

- Without strong fields

steps\β	2.4	3.2	4.54
8	$(-0.0086 \pm 0.0008) * x - 0.0186 \pm 0.0795$	$(-0.0088 \pm 0.0008) * x - 0.0346 \pm 0.0860$	$(-0.0089 \pm 0.0009) * x - 0.0522 \pm 0.0934$
16	$(-0.0079 \pm 0.0007) * x - 0.0284 \pm 0.0730$	$(-0.0080 \pm 0.0008) * x - 0.0451 \pm 0.0791$	$(-0.0080 \pm 0.0008) * x - 0.0645 \pm 0.0859$
32	$(-0.0072 \pm 0.0006) * x - 0.0353 \pm 0.0674$	$(-0.0073 \pm 0.0007) * x - 0.0520 \pm 0.0724$	$(-0.0072 \pm 0.0007) * x - 0.0746 \pm 0.0778$

TABLE V. PIMC-QA without strong fields

steps\β	2.4	3.2	4.54
8	$(-0.0238 \pm 0.0010) * x - 0.3787 \pm 0.0906$	$(-0.0241 \pm 0.0012) * x - 0.4207 \pm 0.1063$	$(-0.0239 \pm 0.0014) * x - 0.4530 \pm 0.1232$
16	$(-0.0219 \pm 0.0009) * x - 0.3369 \pm 0.0792$	$(-0.0220 \pm 0.0010) * x - 0.3587 \pm 0.0904$	$(-0.0214 \pm 0.0012) * x - 0.3822 \pm 0.1036$
32	$(-0.0202 \pm 0.0008) * x - 0.3012 \pm 0.0705$	$(-0.0200 \pm 0.0009) * x - 0.3122 \pm 0.0772$	$(-0.0190 \pm 0.0009) * x - 0.3147 \pm 0.0850$

TABLE VI. PIMC-QA with strong fields

  - Ratios between SVMC without χ-correction and D-Wave
    - Min: 1.4423 (at $steps = 512$, $\beta = 2.4$)
    - Max: 1.9808 (at $steps = 128$, $\beta = 4.54$)
  - Ratios between SVMC with χ-correction and D-Wave
    - Min: 1.2692 (at $steps = 512$, $\beta = 2.4$)
    - Max: 1.8269 (at $steps = 128$, $\beta = 4.54$)
  - Ratios between PIMC-QA and D-Wave
    - Min: 1.3846 (at $steps = 32$, $\beta = 2.4$)
    - Max: 1.7115 (at $steps = 8$, $\beta = 4.54$)

- With strong fields
  - Ratios between SVMC without χ-correction and D-Wave
    - Min: 2.0818 (at $steps = 512$, $\beta = 2.4$)
    - Max: 2.9091 (at $steps = 128$, $\beta = 4.54$)
  - Ratios between SVMC with χ-correction and D-Wave
    - Min: 1.7000 (at $steps = 512$, $\beta = 2.4$)
    - Max: 2.4273 (at $steps = 128$, $\beta = 4.54$)
  - Ratios between PIMC-QA and D-Wave
    - Min: 1.7273 (at $steps = 32$, $\beta = 4.54$)
    - Max: 2.1909 (at $steps = 8$, $\beta = 3.2$)

Appendix D: Chi probe for SVMC

The single qubit Hilbert space modeled as a spin vector in the SVMC numerics is obtained from the two lowest energy wave functions of the continuous flux qubit Hamiltonian with zero flux body bias (see App. A). For sufficiently high flux body bias, these two wave functions start mixing with higher energy wave functions of the continuous flux qubit Hamiltonian. We have checked that, up to the freezing point, the flux bias remains low for the problems that we study in this paper. Nevertheless, a model introduced by D-Wave to deal with this error has been treated as a fitting parameter for SVMC numerics in previous works [42, 43]. Our own derivation of this model gives the following equations modifying the couplings and local fields of the original Hamiltonian

$$h'_i = h_i - \chi \sum_j J_{ij} h_j \tag{D1}$$

$$J'_{ij} = J_{ij} - 2\chi \sum_k J_{ik} J_{kj} \ . \tag{D2}$$

While these equations are slightly different from those used in other works [42, 43], their effect is the same for the problems under study here. Explicitly, the problem becomes more ferromagnetic, and this has the effect of decreasing the barrier height for $h_1 < J/2$.

We want to constraint the possible values of χ consistent with SVMC when χ is treated as a fitting parameter. To that effect we introduce a "chi-probe" problem related to the weak-strong cluster "motive", but without a multi-spin energy barrier. We also introduce many extra nearest-neighbor ferromagnetic couplings to increase

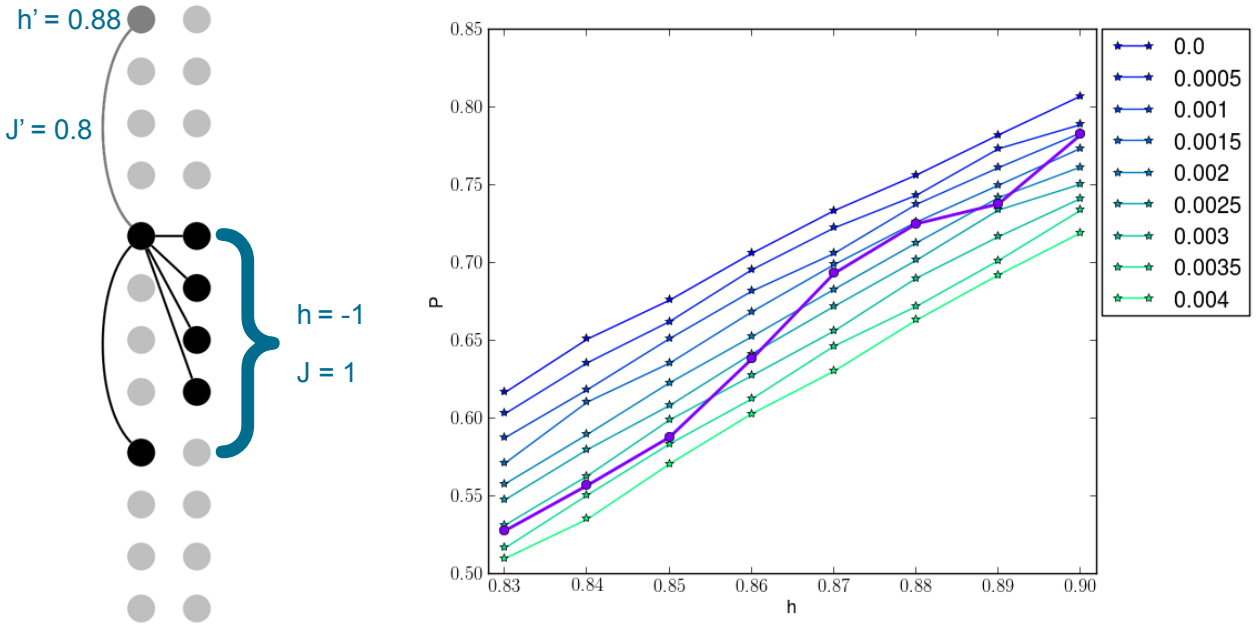

(a) Chi-probe problem

(b) Chi-probe probabilities

FIG. 32. Problem to constraint values of χ compatible with SVMC. (a) Layout of the problem. (b) D-Wave data success probabilities (thicker line with $\circ$ markers) and SVMC success probability for the "chi-probe" problems. The lines with $\star$ markers correspond to SVMC with different values of χ, from 0 to 0.004. The minimum residual error is found for $\chi = 0.0025$. We use SVMC with 125K sweeps and T=15 mK, as explained in the main text.

the sensitivity cross-talk of Eq. (D2). Figure 32a shows the layout of this problem. Figure 32b shows the D-Wave data success probabilities and SVMC success probabilities for the "chi-probe" problems. The minimum residual error is found for $\chi = 0.0025$, and we use this value of χ in the main text when appropriate. Because our factor of 2 in Eq. (D2) this value of χ is roughly equivalent to a value of 0.05 for the equations used in Ref. [42].

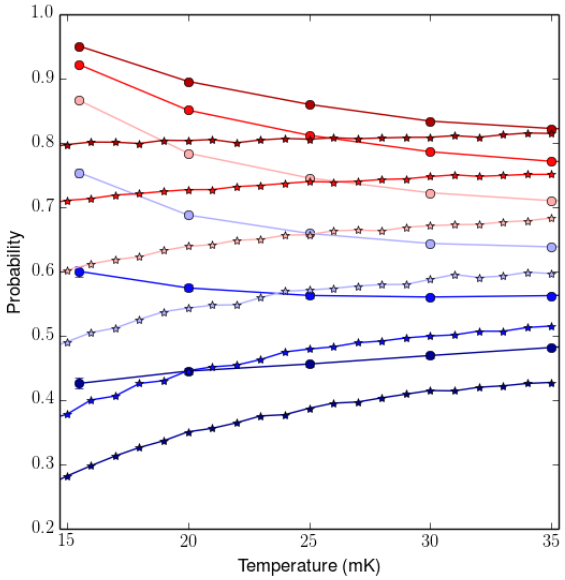

FIG. 33. Probability of success versus temperature for D-Wave data ($\circ$ markers) and SVMC numerics ($\Diamond$ markers). We plot (from top to bottom, and red to blue) $h_1 = [0.38, 0.4, 0.42, 0.44, 0.46, 0.48]$. Error bars are smaller than markers. We use SVMC with $\chi = 0.0025$ and 15 mK algorithmic temperature for 128K sweeps, as explained in the text.

Figure 33 shows a comparison of D-Wave data and SVMC numerics with $\chi = 0.0025$ (compare with Fig. 18).

As explained in the text, we choose 128K sweeps for an algorithmic temperature of 15 mK. Crucially, the temperature dependence is still the opposite for SVMC with χ than for the D-Wave data, as expected. Figure 34a shows the success probability as a function of temperature for D-Wave, open system quantum numerics and the classical paths model (SVMC) for $h_1 = 0.44$ in the Hamiltonian of Eq. (4). We include SVMC with $\chi = 0.0025$. The probability of success is higher for SVMC with than without χ. The reason is that the problem modified with χ is more ferromagnetic: it has an effectively lower ratio h_1/J. Nevertheless, the probability of success for SVMC with χ is still lower than the probability of success for D-Wave. Figure 34b shows the probability of success versus $h_1 = [0.38, 0.4, 0.42, 0.44, 0.46, 0.48, 0.52, 0.54, 0.56, 0.58, 0.6]$.

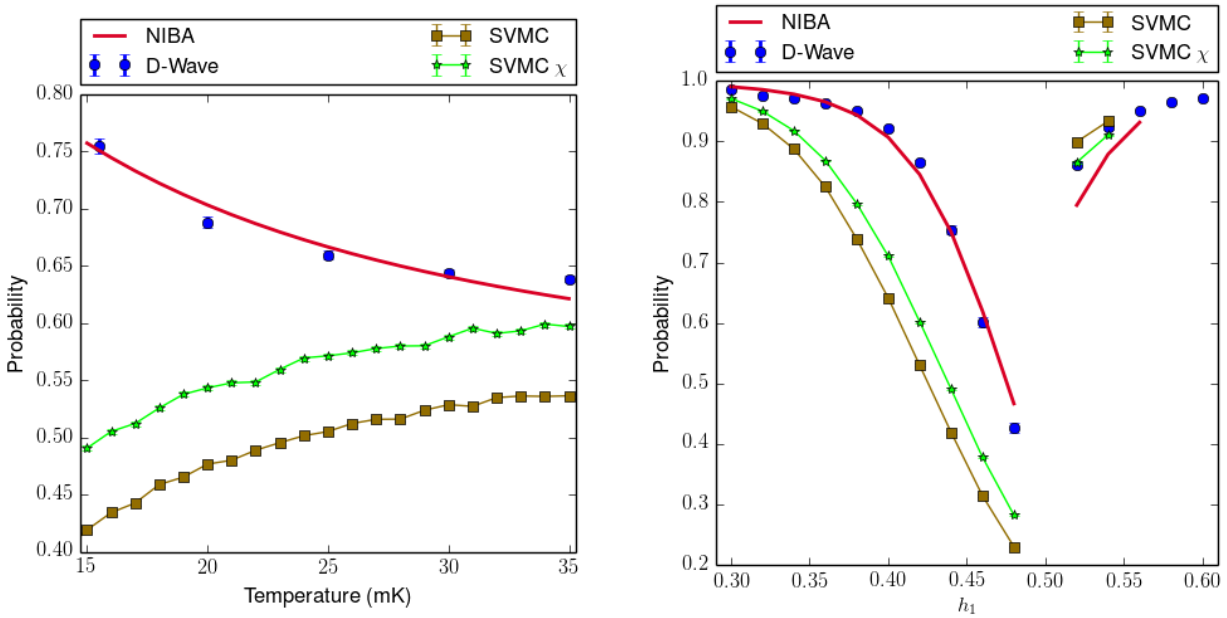

(a) Probability vs. T for $h_1 = 0.44$.

(b) Probability vs. h_1.

FIG. 34. Plots including SVMC with $\chi = 0.0025$ for the double well potential problem introduced in the main text. (a) Probability of success versus temperature at $h_1 = 0.44$ for D-Wave (purple $\circ$ marker), the NIBA Quantum Master Equations (continuous red line) and the classical paths model (SVMC). The two SVMC curves correspond to SVMC (brown $\square$ marker) and SVMC with $\chi = 0.0025$ (green $\star$ marker). (b) Probability of success versus h_1. Error bars are smaller than markers.

[1] G. Gamow, Z. Physik **51** (1928).
[2] A. B. Finnila, M. A. Gomez, C. Sebenik, C. Stenson, and J. Doll, Chem. Phys. Lett. , 343 (1994).
[3] T. Kadowaki and H. Nishimori, Phys. Rev. E **58**, 5355 (1998).
[4] J. Brooke, D. Bitko, T. F. Rosenbaum, and G. Aeppli, Science **284**, 779 (1999).
[5] E. Farhi, J. Goldstone, and S. Gutmann, quant-ph/0201031 (2002).
[6] G. E. Santoro, R. Martoňák, E. Tosatti, and R. Car, Science **295**, 2427 (2002).
[7] M. Johnson, M. Amin, S. Gildert, T. Lanting, F. Hamze, N. Dickson, R. Harris, A. Berkley, J. Johansson, P. Bunyk, *et al.*, Nature **473**, 194 (2011).
[8] T. Lanting, R. Harris, J. Johansson, M. H. S. Amin, A. J. Berkley, S. Gildert, M. W. Johnson, P. Bunyk, E. Tolkacheva, E. Ladizinsky, N. Ladizinsky, T. Oh, I. Perminov, E. M. Chapple, C. Enderud, C. Rich, B. Wilson, M. C. Thom, S. Uchaikin, and G. Rose, Physical Review B **82**, 060512 (2010).
[9] J. G. Edward Farhi1, *, S. Gutmann, J. Lapan, A. Lundgren, and D. Preda, Science **292**, 472 (2001).
[10] R. Harris, J. Johansson, A. J. Berkley, M. W. Johnson, T. Lanting, S. Han, P. Bunyk, E. Ladizinsky, T. Oh, I. Perminov, E. Tolkacheva, S. Uchaikin, E. M. Chapple, C. Enderud, C. Rich, M. Thom, J. Wang, B. Wilson, and G. Rose, Physical Review B **81** (2010), 10.1103/PhysRevB.81.134510.
[11] R. Harris, M. W. Johnson, T. Lanting, A. J. Berkley, J. Johansson, P. Bunyk, E. Tolkacheva, E. Ladizinsky, N. Ladizinsky, T. Oh, F. Cioata, I. Perminov, P. Spear, C. Enderud, C. Rich, S. Uchaikin, M. C. Thom, E. M. Chapple, J. Wang, B. Wilson, M. H. S. Amin, N. Dickson, K. Karimi, B. Macready, C. J. S. Truncik, and G. Rose, Physical Review B **82**, 024511 (2010).
[12] J. M. Martinis, K. B. Cooper, R. McDermott, M. Steffen, M. Ansmann, K. D. Osborn, K. Cicak, S. Oh, D. P. Pappas, R. W. Simmonds, and C. C. Yu, Phys. Rev. Lett. **95**, 210503 (2005).
[13] L. Faoro and L. Ioffe, Phys. Rev. Lett. , 227995 (2008).
[14] E. Paladino, Y. Galperin, G. Falci, and B. Altshuler, Reviews of Modern Physics **86**, 361 (2014).
[15] P. Ao and J. Rammer, Phys. Rev. Lett. **62**, 3004 (1989).
[16] Y. Kayanuma and H. Nakayama, Physics Review B

57, 13099 (1998).
[17] T. Lanting, M. H. S. Amin, M. W. Johnson, F. Altomare, A. J. Berkley, S. Gildert, R. Harris, J. Johansson, P. Bunyk, E. Ladizinsky, E. Tolkacheva, and D. V. Averin, Phys. Rev. B **83**, 180502 (2011).
[18] The same Hamiltonian is obtained in the basis of Spin coherent states identifying $q_k = \cos\theta_k$ and each spin operator S^α with its expectation value.
[19] F. K. Wilhelm, M. J. Storcz, U. Hartmann, and M. R. Geller, in *Manipulating Quantum Coherence in Solid State Systems*, Vol. 244 (Springer Netherlands, 2007) pp. 195–232.
[20] A. J. Leggett, S. Chakravarty, A. Dorsey, M. P. Fisher, A. Garg, and W. Zwerger, Reviews of Modern Physics **59**, 1 (1987).
[21] T. Albash, S. Boixo, D. A. Lidar, and P. Zanardi, New J. Phys. **14**, 123016 (2012).
[22] M. S. Sarandy and D. A. Lidar, Phys. Rev. Lett **95**, 250503 (2005).
[23] M. S. Sarandy and D. A. Lidar, Phys. Rev. A **95**, 012331 (2005).
[24] M. Amin, P. Love, and C. Trunci, Phys. Rev. Lett **100**, 06050 (2008).
[25] I. de Vega, M. C. B. nuls, and A. Pérez, Phys. Rev. Lett **12**, 123010 (2010).
[26] M. Amin, C. Truncik, and D. Averin, Phys. Rev. A **80**, 022303 (2009).
[27] S. Sendelbach, D. Hover, A. Kittel, M. Mck, J. M. Martinis, and R. McDermott, Phys. Rev. B **67**, 094510 (2003).
[28] D. V. Harlingen, T. Robertson, B. Plourde, P. Reichardt, T. Crane, and J. Clarke, Phys. Rev. B **70**, 064517 (2004).
[29] S. Sendelbach, D. Hover, A. Kittel, M. Mck, J. M. Martinis, and R. McDermott, Phys. Rev. Lett. **100**, 227006 (2008).
[30] J. Bylander, S. Gustavsson, F. Yan, F. Yoshihara, K. Harrabi, G. Fitch, D. G. Cory, Y. Nakamura, J.-S. Tsai, and W. D. Oliver, Naure Physics **7**, 565 (2011).
[31] F. Yan, J. Bylander, S. Gustavsson, F. Yoshihara, K. Harrabi, D. G. Cory, T. P. Orlando, Y. Nakamura, J.-S. Tsai, and W. D. Oliver, Phys. Rev. B **85**, 17452 (2012).
[32] F. Yoshihara, Y. Nakamura, F. Yan, S. Gustavsson, J. Bylander, W. D. Oliver, and J.-S. Tsai, Phys. Rev. B **89**, 020503 (2014).
[33] R. Harris, M. Johnson, S. Han, A. Berkley, J. Johansson, P. Bunyk, E. Ladizinsky, S. Govorkov, M. Thom, S. Uchaikin, B. Bumble, A. Fung, A. Kaul, A. Kleinsasser, M. Amin, and D. Averin., Phys. Rev.Lett. **101**, 117003 (2008).
[34] M. H. S. Amin and D. V. Averin, Phys. Rev. Lett. **100**, 197001 (2008).
[35] A. J. Leggett, S. Chakravarty, A. T. Dorsey, M. P. A. Fisher, A. Garg, and W. Zwerger, Reviews of Modern Physics **59**, 1 (1987).
[36] M. H. S. Amin, D. V. Averin, and J. A. Nesteroff, Physical Review A **79**, 022107 (2009).
[37] W. H. Zurek, Phys. Rev. D , 1516 (1981).
[38] P. Ao and J. Rammer, Phys. Rev. B **43**, 5397 (1991).
[39] H. Dekker, Physics Review A **35**, 1436 (1987).
[40] R. Marcus, J. Chem. Phys. **24**, 966 (1956).
[41] S. W. Shin, G. Smith, J. A. Smolin, and U. Vazirani, arXiv preprint arXiv:1401.7087 (2014).
[42] W. Vinci, T. Albash, A. Mishra, P. A. Warburton, and D. A. Lidar, arXiv preprint arXiv:1403.4228 (2014).
[43] T. Albash, T. F. Rønnow, M. Troyer, and D. A. Lidar, arXiv preprint arXiv:1409.3827 (2014).
[44] P. Crowley, T. Duric, W. Vinci, P. Warburton, and A. Green, arXiv preprint arXiv:1405.5185 (2014).
[45] S. Boixo, T. F. Rønnow, S. V. Isakov, Z. Wang, D. Wecker, D. A. Lidar, J. M. Martinis, and M. Troyer, Nature Physics **10**, 218 (2014).
[46] T. F. Rønnow, Z. Wang, J. Job, S. Boixo, S. V. Isakov, D. Wecker, J. M. Martinis, D. A. Lidar, and M. Troyer, Science **345**, 420 (2014).
[47] W. H. Zurek, Prog. Theor. Phys. , 281 (1993).
[48] R. Harris, T. Lanting, A. J. Berkley, J. Johansson, M. W. Johnson, P. Bunyk, E. Ladizinsky, N. Ladizinsky, T. Oh, and S. Han, Phys. Rev. B **80**, 052506 (2009).
[49] M. Enz and R. Schilling, Journal of Physics C: Solid State Physics **19**, 1765 (1986).
[50] A. Boulatov and V. N. Smelyanskiy, Physical Review A **68** (2003), 10.1103/PhysRevA.68.062321, arXiv: quant-ph/0309150.